Design of multimodal antibiotics using deep learning

Angela Cesaro[1-4], Fangping Wan[1-4], Marcelo D. T. Torres[1-4], and Cesar de la Fuente-Nunez[1-4]*

Affiliations

[1]Machine Biology Group, Departments of Psychiatry and Microbiology, Institute for Biomedical Informatics, Institute for Translational Medicine and Therapeutics, Perelman School of Medicine, University of Pennsylvania; Philadelphia, Pennsylvania, United States of America.

[2]Departments of Bioengineering and Chemical and Biomolecular Engineering, School of Engineering and Applied Science, University of Pennsylvania; Philadelphia, Pennsylvania, United States of America.

[3]Department of Chemistry, School of Arts and Sciences, University of Pennsylvania; Philadelphia, Pennsylvania, United States of America.

[4]Penn Institute for Computational Science, University of Pennsylvania; Philadelphia, Pennsylvania, United States of America.

*Corresponding author. Email: cfuente@upenn.edu

Abstract

The rise of antimicrobial resistance has rendered many treatments ineffective, posing serious public health challenges. Intracellular infections are particularly difficult to treat since conventional antibiotics fail to neutralize pathogens hidden within human cells. However, designing molecules that penetrate human cells with preserved antimicrobial activity has historically been a major challenge. Here, we introduce ApexDuo, a multimodal artificial intelligence (AI) model for generating peptides with both cell-penetrating and antimicrobial properties. From a library of 50 million AI-generated compounds, we selected and characterized several candidates. Our lead, Turingcin-46, penetrated mammalian cells and reduced intracellular *Staphylococcus aureus* and *Listeria monocytogenes*. In mouse models of skin abscess and peritonitis, Turingcin-46 reduced bacterial loads by up to two orders of magnitude. In sum, ApexDuo generated multimodal peptide antibiotics, opening new avenues for designing molecules with more than one function.

Introduction

Antimicrobial resistance is a critical global health threat, with nearly three million infections caused by resistant pathogens occurring annually in the United States alone, resulting in over 35,000 deaths and treatment costs exceeding $4.6 billion [1,2]. As pathogenic bacteria evolve diverse resistance mechanisms, they can also employ strategies to evade both host immune defenses and conventional antibiotics. Among these strategies is intracellular pathogenicity, wherein certain bacterial species, such as *Staphylococcus aureus*, invade mammalian cells, replicate intracellularly, and subsequently re-emerge to infect new tissues. This process can lead to severe conditions, including sepsis [3–5]. Addressing this challenge requires novel therapeutics that combine multiple and complementary biological activities.

Traditional drug discovery strategies have proven time-consuming, costly, and increasingly inadequate for addressing the escalating resistance problem. Moreover, these methods predominantly target extracellular bacteria, failing to address the pressing need for therapies capable of eradicating intracellular pathogens [6,7].

Here, we introduce ApexDuo, a deep learning model designed to generate peptide candidates with both cell-penetrating and antimicrobial properties. Cell penetrating peptides (CPPs) facilitate the translocation of biomolecules, including therapeutics, into mammalian cells, while antimicrobial peptides (AMPs) offer broad-spectrum antimicrobial activity against diverse pathogens and may modulate immune responses [8–10]. Our objective was to create novel, multimodal molecules capable of penetrating host cells and reducing intracellular bacteria, thereby addressing critical gaps in the treatment of persistent intracellular infections.

Using ApexDuo, we generated a library of 50 million peptide candidates, synthesized and experimentally tested 60 sequences —collectively termed Turingcins in honor of Alan Turing. Among these, one peptide, Turingcin-46, exhibited remarkable efficacy in suppressing intracellular *S. aureus* infections *in vitro*. Finally, we provide evidence that Turingcin-46 displays anti-infective activity in two different mouse models.

Results

Overview of ApexDuo

To design peptides with dual cell-penetrating and antimicrobial properties, we leveraged a deep generative model, specifically a maximum mean discrepancy variational autoencoder (MMD-VAE), to produce novel peptide sequences. We then applied deep learning-based predictors to assess both cell-penetrating and antimicrobial activities, identifying candidates with the desired multimodal profiles **(Figure 1A)**. From ~50 million peptides generated, we applied stringent filtering criteria to select 60 top-ranked compounds for synthesis and characterization **(Figure S1A**, see also "**Peptide selection**" subsection of the **Methods)**. These criteria included excluding peptides with high median MIC values, low cell-penetration probabilities, duplicates, and peptides already present in in-house datasets and public databases, as well as minimizing sequence redundancy. After applying these filters, 52 soluble peptides—collectively termed Turingcins—were selected for experimental testing **(Table S1)**.

Composition and physicochemical features of multimodal candidates

To investigate the distribution and similarity of the generated multimodal candidates, we used first token embeddings from the pretrained protein large language model ESM2 to represent peptides from various sources, including non-AMPs/CPPs, AMPs/CPPs, generated peptides, and synthesized peptides. These representations were plotted in 2D using Uniform Manifold Approximation and Projection (UMAP), revealing that the generated multimodal candidates overlapped with known AMPs/CPPs. This overlap suggests their potential to exhibit both antimicrobial and cell-penetrating properties **(Figure 1B)**.

An analysis of amino acid composition revealed distinctive features of Turingcins. These peptides showed slight enrichments in isoleucine, lysine, leucine, and asparagine frequencies, contributing to their higher net positive charge relative to common AMPs and CPPs, which generally exhibit lower lysine levels. Conversely, Turingcins displayed reduced levels of cysteine, aspartic acid, glutamic acid, and glycine, as well as lower arginine content compared to CPPs, and lower valine content compared to AMPs. Notably, the synthesized and validated Turingcins lacked cysteine, aspartic acid, and proline residues altogether **(Figure 1C)**.

Regarding physicochemical properties, the multimodal candidates demonstrated lower normalized hydrophobicity values compared to known AMPs and CPPs but exhibited intermediate amphiphilicity index values—an important trait for peptides designed to penetrate biological membranes **(Figures 1D-G)**. This suggests their membrane interactions are less intense than those of highly amphiphilic peptides. The Turingcins showed intermediate values for amphiphilicity, hydrophobicity, and disordered conformation propensity, bridging the characteristics of AMPs and CPPs. However, their net charge, hydrophobic residue angle, and isoelectric point aligned more closely with CPPs, while other features more closely resembled AMPs **(Figures 1D-G and S1B-I).**

These distinct physicochemical and compositional features set Turingcins apart from previously described peptide classes, highlighting their unique potential as multimodal therapeutics.

In vitro antimicrobial activity of multimodal candidates

The antimicrobial efficacy of the designed Turingcins was initially evaluated against twelve clinically relevant bacterial strains, encompassing both Gram-positive and Gram-negative species, with a focus on members of the ESKAPEE group—recognized by the World Health Organization as major public health threats [11] **(Figure 2B)**. A remarkable 90.38% (47/52) of Turingcins exhibited activity against at least one pathogen with MIC values (minimal inhibitory concentrations resulting in complete inhibition of microbial growth) ranging from 0.78 to 50 μmol L^{-1}. Among these, 15 peptides demonstrated activity against *S. aureus* ATCC 12600.

Due to its ability to invade host cells, establish persistent colonization, and cause recurrent infections by replicating within both phagocytic and non-phagocytic cells [12], *S. aureus* was selected as an intracellular pathogen for experimental characterization in this study.

122 **Mechanism of action of Turingcins**

123 To explore the antimicrobial mechanisms of the 15 Turingcins active against *S. aureus*
124 ATCC 12600, we assessed their ability to depolarize bacterial membranes, a typical target
125 of AMPs through non-specific lipid bilayer interactions [13] **(Figures 2C and S2A)**. Using
126 the voltage-sensitive dye $DiSC_3$-5, which fluoresces upon membrane depolarization, we
127 identified significant perturbations in membrane potential in the case of five peptides
128 (Turingcins 34, 35, 37, 57, and 58), representing 33% of those tested.

129 In contrast, nine active peptides (53%; Turingcins 2, 8, 12, 15, 17, 22, 23, 46, and 47)
130 exhibited minimal or no significant fluorescence changes, suggesting alternative
131 antimicrobial mechanisms. Interestingly, Turingcin-28 reduced the fluorescence of the
132 probe, a phenomenon potentially linked to its high tryptophan content (6 out of 18
133 residues, 33%), the highest among the tested sequences **(Figures 2C and S2A)**.

134 This diversity in mechanisms of action highlights the algorithm's ability to generate
135 peptides with multifaceted antimicrobial strategies, reflecting a versatile approach to
136 addressing infections.

137

138 ***In vitro* cytotoxicity and hemolytic activity**

139 Evaluating the potential toxicities of Turingcins is a critical step in assessing their
140 bioactivity and therapeutic potential. To assess their toxicity, we conducted dose-response
141 3-(4, 5-dimethylthiazolyl-2)-2,5-diphenyltetrazolium bromide (MTT) cytotoxicity assays
142 using immortalized human keratinocytes (HaCaT) and phorbol 12-myristate 13-acetate
143 (PMA)-differentiated human monocytes (THP-1), modeling macrophages [14,15]. These
144 assays assessed the biocompatibility of 43 antimicrobial Turingcins with both non-
145 phagocytic and phagocytic cells **(Figures 2D, S2B and S2C; Table S2)**. CC_{50} values (the
146 concentration causing 50% cell death) were determined through non-linear regression of
147 dose-response data (3.12–50 μmol L^{-1}) and compared to their corresponding MIC values
148 **(Figures 2D, S2B and S2C; Table S2)**.

149 In HaCaT cells, 9.3% of Turingcins (4 out of 43) showed CC_{50} values below 12.5 μmol
150 L^{-1}, compared to only 3% (1 out of 43) in PMA-differentiated THP-1 cells, indicating
151 greater susceptibility of keratinocytes than macrophages to Turingcins. Nearly all
152 peptides exhibited CC_{50} values at least twice their MIC, except Turingcin-32, whose
153 antimicrobial effective dose (50 μmol L^{-1}) exceeded its CC_{50} against HaCaT cells (34.84
154 μmol L^{-1}).

155 To further assess safety, we evaluated the hemolytic activity of Turingcins by exposing
156 red blood cells (RBCs) to the peptides, a standard method for toxicity evaluation of
157 antimicrobial agents [15]. Four of the 43 Turingcins tested (9.3%) displayed hemolytic
158 concentration causing 50% cell death (HC_{50}) at values below 12.5 μmol L^{-1} **(Figures 2D**
159 **and S2D; Table S2)**.

160 These findings highlight the promising safety profile of ApexDuo-designed compounds.
161 Most Turingcins demonstrated CC_{50} or HC_{50} values that exceeded their MIC by 2 to over
162 50 times and surpassed 100 times in the case of RBCs. These findings underscore the
163 success of ApexDuo in balancing antimicrobial potency with minimal host cell toxicity.

164

165 **Secondary structure of Turingcins**

166 The secondary structures of short peptides are inherently dynamic, often shifting between
167 disordered and ordered states at hydrophobic-hydrophilic interfaces. For AMPs, this
168 structural plasticity is crucial for their interaction with biological membranes, as it
169 underlies their functional mechanisms of action [16]. Likewise, recent studies indicate that
170 the secondary structural properties and conformations of CPPs profoundly influence their
171 cellular uptake pathways and overall internalization efficiency, underscoring the
172 importance of peptide structure in determining both antimicrobial and cell-penetrative
173 activities [17].

174 To characterize the secondary structure of the synthesized Turingcins, Circular Dichroism
175 (CD) spectroscopy was performed in various environments: water, trifluoroethanol (TFE)
176 in water mixture (3:2, v:v), methanol (MeOH) in water mixture (1:1, v:v), and sodium
177 dodecyl sulfate (SDS) in water (10 mmol L^{-1}). The TFE/water and MeOH/water mixtures
178 were used to induce distinct secondary structures: TFE usually promotes α-helical
179 conformations by dehydrating peptide amide groups and facilitating intramolecular
180 hydrogen bonds, while MeOH favors β-sheet conformations by interacting with the amide
181 groups of the backbone and favoring intermolecular side chains interactions. SDS
182 micelles were included to mimic the bilayer environment of biological membranes and
183 provide insight into how the peptides might behave *in vivo* [18–20].

184 All Turingcins were analyzed using CD spectroscopy over a wavelength range of 260 to
185 190 nm **(Figures 2E and S3).** Secondary structure fractions were estimated using the
186 BeStSel server [21]. In water, most peptides were predominantly unstructured. Notably,
187 however, the inactive peptides Turingcins 1, 7, and 21 showed a pronounced tendency to
188 adopt α-helical structures (31.4%, 39%, and 29.5%, respectively). In TFE and water
189 mixture, unstructured conformations remained dominant, whereas in MeOH and water
190 mixture, peptides displayed enhanced β-like structural features. In the presence of SDS
191 micelles in water, which are intended to simulate membrane-like environments, the
192 unstructured state generally predominated, with certain peptides exceeding 65%
193 unstructured content **(Figures 2E and S3).** In summary, Turingcins are generally
194 unstructured and tend to β-like conformations in β-inducer medium.

195

196 **Intracellular antimicrobial activity of Turingcins**

197 To evaluate the intracellular antimicrobial activity of the most promising Turingcins, we
198 developed a model using HaCaT and PMA-differentiated THP-1 cells infected with
199 intracellular *S. aureus* ATCC 12600 **(Figure S4A)**. Gentamicin was used to eliminate
200 extracellular bacteria due to its poor cellular uptake[22–24]. To validate the model, we also
201 tested gentamicin at 5, 100, and 500 μg mL^{-1} and confirmed that it does not eliminate
202 intracellular *S. aureus*, even at the highest concentration tested **(Figure S4B)**.

203 From the MIC panel of Turingcins **(Figure 2B)**, we selected nine highly active candidates
204 against *S. aureus*, testing them in our intracellular antimicrobial activity assays at three
205 concentrations (12.5, 25, and 50 μmol L^{-1}) **(Figures S5A-D)**. This strategy allowed us to
206 identify time-dependent trends while excluding conditions where toxicity obscured
207 antimicrobial efficacy. Two out of the nine Turingcins (i.e., Turingcin-46 and Turingcin-
208 47) tested against intracellular *S. aureus* effectively reduced bacterial loads at nontoxic

concentrations, with particularly strong effects observed at 1 and 3 hours **(Figures 3A and S5E**; see also **S6A** for extracellular bacterial counts**)**.

To expand our studies to a highly relevant intracellular pathogen, we performed additional intracellular antimicrobial assays with *L. monocytogenes*[25,26] using Turingcin-46 and -58, both of which were active against *L. monocytogenes* in MIC assays **(Figure 2B)** and nontoxic against THP-1 cells at the concentrations tested. In these experiments, Turingcin-46, but not Turingcin-58, significantly reduced the intracellular bacterial load compared to untreated controls, confirming its efficacy against intracellular *L. monocytogenes* **(Figures 3B**; see also **S6A** for extracellular bacterial counts**)**.

To further examine Turingcin-46's cell-penetration capabilities and intracellular localization, we conjugated the peptide with Cyanine-5 (Cy5) at the N-terminus and applied it to both infected and uninfected cells. Two concentrations of Cy5-Turingcin-46 (25 and 50 μmol L^{-1}) were tested at 1- and 3-hours post-treatment. Afterward, cells were fixed and stained with Hoechst (blue) to label nuclei and WGA (green) to visualize cell walls, then analyzed by fluorescence microscopy. Substantial intracellular accumulation of Cy5-Turingcin-46 (purple signal) was observed in both infected **(Figures S6C and D)** and uninfected cell monolayers **(Figures 3C and D)**, compared to untreated controls. In contrast, no intracellular signal was detected when using Cy5 alone under the same experimental conditions, except for faint residual fluorescence occasionally observed in infected macrophages at 3 hours at the highest concentration tested, which may reflect nonspecific uptake through phagocytic mechanisms **(Figures S7)**.

Altogether, these findings confirm Turingcin-46's ability to penetrate mammalian cells and effectively kill intracellular pathogens such as *S. aureus* and *L. monocytogenes*.

Ala-scan screening of Turingcin-46 to elucidate structure-function relationships

To dissect the contributions of individual amino acids to Turingcin-46's biological activity, we performed alanine-scan screening. Each residue in Turingcin-46 was systematically replaced with alanine, generating 18 single-substitution variants **(Figures 4, S8 and S9; Table S3)**. Alanine, with its short aliphatic side chain, was chosen to preserve peptide backbone length while minimizing disruptive interactions between side chains [27,28].

Analysis of the antimicrobial and cytotoxic properties of these alanine-substituted variants revealed that mutations at positions 1 (F), 3 (W), 4 (W), 5 (L), 10 (L), 19 (R), 20 (R), and 21 (K) significantly increased the MIC against *S. aureus* ATCC 12600, rendering the peptides inactive **(Figures 4A and S8A)**. Substitutions at positions 15 (I) and 17 (I) also diminished antimicrobial potency, albeit to a lesser degree. These findings highlight the importance of hydrophobic and aliphatic residues such as tryptophan, phenylalanine, leucine, and isoleucine, as well as positively charged arginine and lysine, in mediating antimicrobial effects. Notably, the changes in cationic residues close to the C-terminus were more impactful than close to the N-terminus where cationic residues are surrounded by hydrophobic and aliphatic residues.

Some of the residues affecting MIC values also impacted cytotoxicity **(Figures 4A, S8B and S8C)**. Mutations leading to a loss of antimicrobial activity generally reduced cytotoxicity in PMA-differentiated THP-1 cells (e.g., W4A, L5A, R20A, and K21A). All the derivatives had similar activity profiles or were more toxic than Turingcin-46 against

253 keratinocytes. The wild-type peptide did not present high hemolytic activity, and the Ala-
254 scan screening showed that substitutions that led to enhanced mean hydrophobicity values
255 correlated with a lower propensity for hemolysis **(Figures 4A and S8D; table S4)**.

256 Circular dichroism analysis showed that Turingcin-46 and its alanine-substituted variants
257 generally adopted similar secondary structures **(Figures 4B and S9)**. In aqueous solution,
258 the peptides were predominantly unstructured, with some β-like conformations. In TFE
259 and water mixture, variants that lost antimicrobial activity showed an increased tendency
260 to form α-helical structures (up to 37%). Nevertheless, in MeOH and water mixture and
261 SDS micelles, both wild-type and mutated sequences displayed similar proportions of
262 unstructured and β-like conformations **(Figures 4B and S9A-E)**.

263 To examine how these structural changes affected interactions with biological
264 membranes, we employed two fluorescent probes—$DiSC_3$-5 and $DiBAC_4$-3 [29,30]—to
265 evaluate membrane depolarization in bacterial and eukaryotic cells, respectively.
266 Turingcin-46 had a modest ability to depolarize the bacterial membrane, a trait shared by
267 most alanine-substituted variants **(Figures 4C and S8E)**. Interestingly, I15A- and I17A-
268 substituted Turingcin-46 displayed enhanced depolarizing activity against *S. aureus*
269 membranes **(Figures 4C and S8E)**.

270 The peptides exhibited distinct effects on eukaryotic cell membranes. In HaCaT
271 keratinocytes, Turingcin-46 did not alter membrane potential, whereas most alanine-
272 substituted derivatives induced hyperpolarization (indicated by decreased fluorescence),
273 particularly those mutated at the N- and C-termini. Conversely, K7A- and I15A-
274 substituted variants increased fluorescence, indicating membrane depolarization. In
275 PMA-differentiated THP-1 macrophages, wild-type Turingcin-46 induced membrane
276 depolarization, whereas most alanine-substituted variants showed reduced depolarizing
277 effects **(Figures 4D and S8F-G)**. One exception was K7A-Turingcin-46, which caused
278 significantly greater depolarization than the wild-type sequence. These results underscore
279 the cell-type specificity of peptide-membrane interactions influenced by phospholipid
280 composition.

281 To further assess intracellular antimicrobial activity, we selected the K7A- and K16A-
282 Turingcin-46 variants based on their antimicrobial potency and cytotoxicity profiles,
283 which were comparable to those of the lead peptides. However, K7A-Turingcin-46 did
284 not reduce the intracellular bacterial burden in HaCaT and THP-1 cells when tested at
285 non-cytotoxic concentrations **(Figure 4E;** see also **Figure S9F-G** for extracellular
286 bacteria counts**).** Conversely, K16A-Turingcin-46 preserved intracellular activity in
287 macrophages, although its effectiveness was diminished compared to the lead wild-type
288 sequence **(Figure 4E;** see also **Figure S9F-G** for extracellular bacteria counts**)**. This
289 suggests that these variants lack key sequence features necessary for the full multimodal
290 activity of the wild-type peptide.

291 In summary, alanine-scan screening revealed the importance of Turingcin-46's unique
292 combination and distribution of amino acid residues in mediating its membrane
293 interactions and multifunctional biological activity. This analysis highlights the nuanced
294 interplay between sequence composition and peptide function in computationally
295 designed molecules.

296

297 **Resistance to proteolytic degradation**

298 Before conducting *in vivo* mouse experiments, we assessed Turingcin-46's stability in the
299 presence of serum proteases. After one hour of incubation, approximately 50% of the
300 peptide remained intact. We attribute this stability to the presence of hindered
301 hydrophobic residues such as phenylalanine and tryptophan that may further reduce
302 protease accessibility **(Figure S10A).**

303

304 **Anti-infective efficacy of Turingcin-46 in animal models**

305 To investigate Turingcin-46's antimicrobial efficacy in complex biological environments,
306 we tested it in two mouse models: a skin abscess model and a peritonitis/sepsis model
307 **(Figures 5, S10B-D** and **S11)**.

308 In the skin abscess model, a 20 μL suspension containing 10^7 *S. aureus* ATCC 12600
309 cells in phosphate-buffered saline (PBS) was applied to a wound on the back of the mice
310 [11,31–33] **(Figures 5A, 5B and S10B)**. A single dose of Turingcin-46 was administered
311 directly to the infected area. After 24 hours, the bacterial count decreased by more than
312 two orders of magnitude compared to the untreated control group, with Turingcin-46
313 demonstrating slightly greater potency than gentamicin **(Figure 5B)**. Confocal
314 microscopy of skin samples treated with Cy5-labeled Turingcin-46 confirmed the
315 peptide's cellular penetration capability, showing fluorescence within the stratified
316 squamous epithelium **(Figures 5C and S10C)**. Throughout the experiments, no
317 significant changes in body weight, a general indicator of potential toxicity, were detected
318 **(Figure S10B)**.

319 Next, we evaluated Turingcin-46 in a peritonitis/sepsis mouse model **(Figures 5D, 5E,**
320 **S10D** and **S11A)**, which allows for the evaluation of intracellular antimicrobial activity
321 [34,35]. Mice were intraperitoneally infected with 100 μL containing 5×10^{10} *S. aureus* ATCC
322 12600 cells *per* mL. Two hours post-infection, three doses of Turingcin-46 were
323 administered intraperitoneally at 1.5-hour intervals to mitigate peptide degradation (as
324 confirmed by prior proteolytic stability studies).

325 One day after treatment, Turingcin-46 significantly reduced bacterial burdens in multiple
326 organs, including the liver, kidneys, spleen, lungs, and heart, with reductions ranging
327 from 1.2 to 1.8 orders of magnitude. Notably, Turingcin-46 outperformed gentamicin
328 (positive control) in the liver, spleen, and lungs, suggesting possible organ-specific
329 peptide accumulation. Importantly, no significant changes in body weight were observed,
330 further supporting the peptide's safety at the tested dose **(Figure S10D)**.

331 Gentamicin has poor uptake into mammalian cells, as confirmed by our *in vitro* data
332 **(Figure S4B)** and supported by numerous previous studies [22–24], making it unlikely to act
333 directly on intracellular bacteria. However, varying degrees of positive correlation were
334 observed between intracellular and extracellular bacterial loads across treatment groups
335 *in vivo* **(Figure S11B)**, suggesting that the extracellular burden may influence
336 intracellular load through reinfection. A linear regression analysis revealed that the slope
337 of intracellular versus extracellular bacterial loads was substantially lower in the
338 Turingcin-46 group (0.85) compared to the control (1.03) and gentamicin (1.37) groups,
339 indicating a disproportionately stronger reduction in intracellular bacteria counts in the

Turingcin-46 treatment group. In contrast, the steeper slope observed in gentamicin-treated mice suggests that its apparent effect on intracellular bacteria may primarily result from the reduction of extracellular burden. Moreover, the intracellular-to-extracellular bacterial load ratio in the Turingcin-46 group was 1.74-fold lower than that of the gentamicin group, further supporting Turingcin-46's intracellular antimicrobial activity through this comparative trend **(Figure S11C)**.

Overall, these *in vivo* findings highlight Turingcin-46's potent antibiotic activity under physiological conditions and highlight its potential as a multimodal therapeutic agent against infections.

Discussion

Eliminating intracellular pathogens remains a significant therapeutic challenge. Traditional antibiotics often fail to reach sufficient concentrations within host cells to effectively eradicate intracellular bacteria, and achieving therapeutic intracellular levels frequently requires high, potentially toxic doses [36].

While multimodal models are now widely applied in domains such as chatbots, their use in molecular design has been limited due to the complexity of integrating multiple functionalities into a single molecule. Multimodal molecules offer a promising strategy to overcome these barriers, but their design and optimization using conventional methods have proven difficult.

ApexDuo introduces a dual-objective deep learning framework that generates peptides with both antimicrobial and cell-penetrating activities. Whereas most molecular discovery pipelines optimize a single property, ApexDuo couples predictive models for multiple bioactivities within a unified generative workflow, enabling the rational design of functionally versatile peptides. Although antimicrobial and cell-penetrating properties are often studied separately, they are not mutually exclusive [37,38]. ApexDuo exploits this overlap by deliberately designing peptides that combine both functionalities. The Turingcin series discovered through this approach displays a hybrid chemical profile characteristic of antimicrobial and cell-penetrating peptides, demonstrating the efficacy of the strategy. Looking ahead, the framework can be expanded to incorporate further biological functions, such as immunomodulation, endosomal escape, or subcellular targeting, thereby supporting the programmable design of next-generation therapeutics for complex infectious and inflammatory diseases.

Mutational analysis identified sequence elements critical for Turingcin-46's antimicrobial efficacy and cytotoxic selectivity, correlating these features with the peptide's ability to penetrate mammalian cells, suppress intracellular pathogens, and maintain a favorable cytotoxic profile. Furthermore, *in vivo* experiments demonstrated Turingcin-46's robust antimicrobial efficacy in two mouse models, underscoring its potential therapeutic potential. In summary, ApexDuo demonstrates that AI can be used to design multimodal peptides, opening new avenues for designing molecules with more than one function.

Limitations of the study

Despite the advances outlined here, ApexDuo has limitations. The antimicrobial predictor did not incorporate datasets specifically annotated for intracellular activity, which may have constrained the accuracy of predictions for this context. Similarly, limited publicly available data on CPPs restricted the predictor's training. Future efforts to curate large datasets with intracellularly active peptide and cell-penetration annotations will enhance predictive models and accelerate the discovery of improved multimodal antibiotics. Additionally, our study focused on peptides with confirmed antimicrobial activity for downstream intracellular assays, excluding purely cell-penetrating candidates. Broader testing could provide further insights into the full spectrum of ApexDuo-generated molecules and identify additional promising candidates. Finally, we provide strong evidence that lead candidates (i.e., Turingcin-46), significantly reduce infections in mammalian cells and in murine models. Future studies should more granularly delineate this compound's intracellular targeting across additional mouse models.

Acknowledgments

Research reported in this publication was supported by the NIH R35GM138201 and DTRA HDTRA1-21-1-0014. We thank Dr. Mark Goulian for kindly donating the following strains: *Escherichia coli* AIC221 (*Escherichia coli* MG1655 phnE_2::FRT [control strain for AIC222]) and *Escherichia coli* AIC222 (*Escherichia coli* MG1655 pmrA53 phnE_2::FRT [polymyxin resistant]), and the H-MARC core in the Center for Molecular Studies in Digestive and Liver Diseases (P30 DK050306) for kindly donating strains *Acinetobacter baumannii* ATCC 19606 and *Klebsiella pneumoniae* ATCC 13883. We would like to acknowledge the Center for Molecular Studies in Digestive and Liver Diseases (P30DK050306) and the Molecular Pathology and Imaging Core (RRID: SCR_022420) for their assistance with histology sample preparation. Additionally, we thank the Cell & Developmental Biology Microscopy Core at the Perelman School of Medicine (RRID: SCR_022373) for enabling the use of the Zeiss LSM 980 confocal microscope. We thank Gui-Shuang Ying from the Center for Preventive Ophthalmology and Biostatistics (CPOB) Consulting Service for advice on our statistical analyses. We thank the de la Fuente lab members for insightful discussions, especially Sufen Li, for her assistance with animal experiments. Figures created with Biorender.com are attributed as such. Molecules were rendered using the PyMOL Molecular Graphics System, Version 3.2 Schrödinger, LLC.

Author contributions:

Conceptualization: AC, CFN
Methodology: AC, FW, MDTT, CFN
Experimental investigation: AC, MDTT
Computational investigation: FW
Visualization: AC, FW, MDTT
Funding acquisition: CFN
Supervision: CFN
Formal analysis: AC, FW, MDTT
Writing – original draft: AC, FW, MDTT, CFN

Writing – review & editing: AC, FW, MDTT, CFN

Competing interests:

CFN is a co-founder and scientific advisor to Peptaris, Inc., provides consulting services to Invaio Sciences and is a member of the Scientific Advisory Boards of Nowture S.L., Peptidus, European Biotech Venture Builder and Phare Bio. CFN is also a member of the Advisory Board for the Peptide Drug Hunting Consortium (PDHC). The de la Fuente Lab has received research funding or in-kind donations from United Therapeutics, Strata Manufacturing PJSC, and Procter & Gamble, none of which were used in support of this work. CFN is on the Advisory Board of Cell Reports Physical Science. Marcelo D. T. Torres is a co-founder and scientific advisor to Peptaris, Inc. An invention disclosure associated with this work has been filed. All other authors declare no competing interests.

References

1. Health department Healthcare-associated Infections and Antimicrobial Resistance Programs (2024). Centers for Disease Control and Prevention. https://www.cdc.gov/healthcare-associated-infections/programs/index.html.

2. Naghavi, M., Vollset, S.E., Ikuta, K.S., Swetschinski, L.R., Gray, A.P., Wool, E.E., Robles Aguilar, G., Mestrovic, T., Smith, G., Han, C., et al. (2024). Global burden of bacterial antimicrobial resistance 1990–2021: a systematic analysis with forecasts to 2050. The Lancet *404*, 1199–1226. https://doi.org/10.1016/S0140-6736(24)01867-1.

3. Thakur, A., Mikkelsen, H., and Jungersen, G. (2019). Intracellular pathogens: Host immunity and microbial persistence strategies. Preprint, https://doi.org/10.1155/2019/1356540 https://doi.org/10.1155/2019/1356540.

4. Eisenreich, W., Rudel, T., Heesemann, J., and Goebel, W. (2019). How viral and intracellular bacterial pathogens reprogram the metabolism of host cells to allow their intracellular replication. Preprint, https://doi.org/10.3389/fcimb.2019.00042 https://doi.org/10.3389/fcimb.2019.00042.

5. de la Fuente-Nunez, C., Cesaro, A., and Hancock, R.E.W. (2023). Antibiotic failure: Beyond antimicrobial resistance. Drug Resistance Updates *71*, 101012. https://doi.org/10.1016/j.drup.2023.101012.

6. Peyrusson, F., Varet, H., Nguyen, T.K., Legendre, R., Sismeiro, O., Coppée, J.-Y., Wolz, C., Tenson, T., and Van Bambeke, F. (2020). Intracellular Staphylococcus aureus persisters upon antibiotic exposure. Nat Commun *11*, 2200. https://doi.org/10.1038/s41467-020-15966-7.

7. Cesaro, A., Bagheri, M., Torres, M., Wan, F., and de la Fuente-Nunez, C. (2023). Deep learning tools to accelerate antibiotic discovery. Expert Opin Drug Discov *18*, 1245–1257. https://doi.org/10.1080/17460441.2023.2250721.

8. Gomarasca, M., F. C. Martins, T., Greune, L., Hardwidge, P.R., Schmidt, M.A., and Rüter, C. (2017). Bacterium-Derived Cell-Penetrating Peptides Deliver

467 Gentamicin To Kill Intracellular Pathogens. Antimicrob Agents Chemother *61*,
468 e02545-16. https://doi.org/10.1128/AAC.02545-16.

469 9. Derakhshankhah, H., and Jafari, S. (2018). Cell penetrating peptides: A concise
470 review with emphasis on biomedical applications. Biomedicine &
471 Pharmacotherapy *108*, 1090–1096. https://doi.org/10.1016/j.biopha.2018.09.097.

472 10. Hancock, R.E.W., and Sahl, H.-G. (2006). Antimicrobial and host-defense
473 peptides as new anti-infective therapeutic strategies. Nat Biotechnol *24*, 1551–
474 1557. https://doi.org/10.1038/nbt1267.

475 11. Cesaro, A., Torres, M.D.T., Gaglione, R., Dell'Olmo, E., Di Girolamo, R., Bosso,
476 A., Pizzo, E., Haagsman, H.P., Veldhuizen, E.J.A., de la Fuente-Nunez, C., et al.
477 (2022). Synthetic Antibiotic Derived from Sequences Encrypted in a Protein from
478 Human Plasma. ACS Nano *16*, 1880–1895.
479 https://doi.org/10.1021/acsnano.1c04496.

480 12. Bravo-Santano, N., Ellis, J.K., Mateos, L.M., Calle, Y., Keun, H.C., Behrends, V.,
481 and Letek, M. (2018). Intracellular Staphylococcus aureus Modulates Host Central
482 Carbon Metabolism To Activate Autophagy. mSphere *3*, e00374-18.
483 https://doi.org/10.1128/mSphere.00374-18.

484 13. Benfield, A.H., and Henriques, S.T. (2020). Mode-of-Action of Antimicrobial
485 Peptides: Membrane Disruption vs. Intracellular Mechanisms. Front Med Technol
486 *2*, 610997. https://doi.org/10.3389/fmedt.2020.610997.

487 14. Mohd Yasin, Z.N., Mohd Idrus, F.N., Hoe, C.H., and Yvonne-Tee, G.B. (2022).
488 Macrophage polarization in THP-1 cell line and primary monocytes: A systematic
489 review. Differentiation *128*, 67–82. https://doi.org/10.1016/j.diff.2022.10.001.

490 15. Cesaro, A., Torres, M.D.T., and de la Fuente-Nunez, C. (2022). Methods for the
491 design and characterization of peptide antibiotics. In Methods in Enzymology
492 (Academic Press), pp. 303–326. https://doi.org/10.1016/bs.mie.2021.11.003.

493 16. Ma, X., Wang, Q., Ren, K., Xu, T., Zhang, Z., Xu, M., Rao, Z., and Zhang, X.
494 (2024). A Review of Antimicrobial Peptides: Structure, Mechanism of Action, and
495 Molecular Optimization Strategies. Fermentation *10*, 540.
496 https://doi.org/10.3390/fermentation10110540.

497 17. Eiríksdóttir, E., Konate, K., Langel, Ü., Divita, G., and Deshayes, S. (2010).
498 Secondary structure of cell-penetrating peptides controls membrane interaction
499 and insertion. Biochimica et Biophysica Acta (BBA) - Biomembranes *1798*, 1119–
500 1128. https://doi.org/10.1016/j.bbamem.2010.03.005.

501 18. Luo, P., and Baldwin, R.L. (1997). Mechanism of helix induction by
502 trifluoroethanol: A framework for extrapolating the helix-forming properties of
503 peptides from trifluoroethanol/water mixtures back to water. Biochemistry *36*,
504 8413–8421. https://doi.org/10.1021/bi9707133.

505 19. Pastor, M.T., López de la Paz, M., Lacroix, E., Serrano, L., and Pérez-Payá, E.
506 (2002). Combinatorial approaches: A new tool to search for highly structured β-

507 hairpin peptides. Proceedings of the National Academy of Sciences *99*, 614–619.
508 https://doi.org/10.1073/pnas.012583999.

509 20. Tulumello, D. V., and Deber, C.M. (2009). SDS Micelles as a Membrane-Mimetic
510 Environment for Transmembrane Segments. Biochemistry *48*, 12096–12103.
511 https://doi.org/10.1021/bi9013819.

512 21. Micsonai, A., Moussong, É., Wien, F., Boros, E., Vadászi, H., Murvai, N., Lee,
513 Y.-H., Molnár, T., Réfrégiers, M., Goto, Y., et al. (2022). BeStSel: webserver for
514 secondary structure and fold prediction for protein CD spectroscopy. Nucleic
515 Acids Res *50*, W90–W98. https://doi.org/10.1093/nar/gkac345.

516 22. Gomarasca, M., F. C. Martins, T., Greune, L., Hardwidge, P.R., Schmidt, M.A.,
517 and Rüter, C. (2017). Bacterium-Derived Cell-Penetrating Peptides Deliver
518 Gentamicin To Kill Intracellular Pathogens. Antimicrob Agents Chemother *61*.
519 https://doi.org/10.1128/AAC.02545-16.

520 23. Imbuluzqueta, E., Elizondo, E., Gamazo, C., Moreno-Calvo, E., Veciana, J.,
521 Ventosa, N., and Blanco-Prieto, M.J. (2011). Novel bioactive hydrophobic
522 gentamicin carriers for the treatment of intracellular bacterial infections. Acta
523 Biomater *7*, 1599–1608. https://doi.org/10.1016/j.actbio.2010.11.031.

524 24. Lutwyche, P., Cordeiro, C., Wiseman, D.J., St-Louis, M., Uh, M., Hope, M.J.,
525 Webb, M.S., and Finlay, B.B. (1998). Intracellular Delivery and Antibacterial
526 Activity of Gentamicin Encapsulated in pH-Sensitive Liposomes. Antimicrob
527 Agents Chemother *42*, 2511–2520. https://doi.org/10.1128/AAC.42.10.2511.

528 25. Kortebi, M., Milohanic, E., Mitchell, G., Péchoux, C., Prevost, M.-C., Cossart, P.,
529 and Bierne, H. (2017). Listeria monocytogenes switches from dissemination to
530 persistence by adopting a vacuolar lifestyle in epithelial cells. PLoS Pathog *13*,
531 e1006734. https://doi.org/10.1371/journal.ppat.1006734.

532 26. Radoshevich, L., and Cossart, P. (2018). Listeria monocytogenes: towards a
533 complete picture of its physiology and pathogenesis. Nat Rev Microbiol *16*, 32–
534 46. https://doi.org/10.1038/nrmicro.2017.126.

535 27. Torres, M.D.T., Sothiselvam, S., Lu, T.K., and de la Fuente-Nunez, C. (2019).
536 Peptide Design Principles for Antimicrobial Applications. J Mol Biol *431*, 3547–
537 3567. https://doi.org/10.1016/j.jmb.2018.12.015.

538 28. Ju, X., Chen, X., Du, L., Wu, X., Liu, F., and Yuan, J. (2015). Alanine-Scanning
539 Mutational Analysis of Durancin GL Reveals Residues Important for Its
540 Antimicrobial Activity. J Agric Food Chem *63*, 6402–6409.
541 https://doi.org/10.1021/acs.jafc.5b02114.

542 29. Trofimenko, E., Grasso, G., Heulot, M., Chevalier, N., Deriu, M.A., Dubuis, G.,
543 Arribat, Y., Serulla, M., Michel, S., Vantomme, G., et al. (2021). Genetic, cellular,
544 and structural characterization of the membrane potential-dependent cell-
545 penetrating peptide translocation pore. Elife *10*, e69832.
546 https://doi.org/10.7554/eLife.69832.

547 30. de Souza-Guerreiro, T.C., Huan Bacellar, L., da Costa, T.S., Edwards, C.L.A.,
548 Tasic, L., and Asally, M. (2024). Membrane potential dynamics unveil the promise
549 of bioelectrical antimicrobial susceptibility Testing (BeAST) for anti-fungal
550 screening. mBio *15*, e0130224. https://doi.org/10.1128/mbio.01302-24.

551 31. Torres, M.D.T., Melo, M.C.R., Flowers, L., Crescenzi, O., Notomista, E., and de
552 la Fuente-Nunez, C. (2022). Mining for encrypted peptide antibiotics in the human
553 proteome. Nat Biomed Eng *6*, 1451–1451. https://doi.org/10.1038/s41551-022-
554 00967-2.

555 32. Torres, M.D.T., Brooks, E.F., Cesaro, A., Sberro, H., Gill, M.O., Nicolaou, C.,
556 Bhatt, A.S., and de la Fuente-Nunez, C. (2024). Mining human microbiomes
557 reveals an untapped source of peptide antibiotics. Cell *187*, 5453-5467.e15.
558 https://doi.org/10.1016/j.cell.2024.07.027.

559 33. Torres, M.D.T., Cesaro, A., and de la Fuente-Nunez, C. (2024). Peptides from non-
560 immune proteins target infections through antimicrobial and immunomodulatory
561 properties. Trends Biotechnol, 0167–7799.
562 https://doi.org/10.1016/j.tibtech.2024.09.008.

563 34. Wang, X., Wang, X., Teng, D., Mao, R., Hao, Y., Yang, N., Li, Z., and Wang, J.
564 (2018). Increased intracellular activity of MP1102 and NZ2114 against
565 Staphylococcus aureus in vitro and in vivo. Sci Rep *8*, 4204.
566 https://doi.org/10.1038/s41598-018-22245-5.

567 35. Sandberg, A., Hessler, J.H.R., Skov, R.L., Blom, J., and Frimodt-Møller, N.
568 (2009). Intracellular Activity of Antibiotics against *Staphylococcus aureus* in a
569 Mouse Peritonitis Model. Antimicrob Agents Chemother *53*, 1874–1883.
570 https://doi.org/10.1128/AAC.01605-07.

571 36. Cruz, G.S., Santos, A.T. dos, Brito, E.H.S. de, and Rádis-Baptista, G. (2022). Cell-
572 Penetrating Antimicrobial Peptides with Anti-Infective Activity against
573 Intracellular Pathogens. Antibiotics *11*, 1772.
574 https://doi.org/10.3390/antibiotics11121772.

575 37. Cruz, G.S., Santos, A.T. dos, Brito, E.H.S. de, and Rádis-Baptista, G. (2022). Cell-
576 Penetrating Antimicrobial Peptides with Anti-Infective Activity against
577 Intracellular Pathogens. Antibiotics *11*, 1772.
578 https://doi.org/10.3390/antibiotics11121772.

579 38. Bahnsen, J.S., Franzyk, H., Sandberg-Schaal, A., and Nielsen, H.M. (2013).
580 Antimicrobial and cell-penetrating properties of penetratin analogs: Effect of
581 sequence and secondary structure. Biochimica et Biophysica Acta (BBA) -
582 Biomembranes *1828*, 223–232. https://doi.org/10.1016/j.bbamem.2012.10.010.

583 39. Pirtskhalava, M., Amstrong, A.A., Grigolava, M., Chubinidze, M., Alimbarashvili,
584 E., Vishnepolsky, B., Gabrielian, A., Rosenthal, A., Hurt, D.E., and Tartakovsky,
585 M. (2021). DBAASP v3: database of antimicrobial/cytotoxic activity and structure
586 of peptides as a resource for development of new therapeutics. Nucleic Acids Res
587 *49*, D288–D297. https://doi.org/10.1093/nar/gkaa991.

40. Suzek, B.E., Huang, H., McGarvey, P., Mazumder, R., and Wu, C.H. (2007). UniRef: comprehensive and non-redundant UniProt reference clusters. Bioinformatics *23*, 1282–1288. https://doi.org/10.1093/bioinformatics/btm098.

41. Wang, G., Li, X., and Wang, Z. (2016). APD3: the antimicrobial peptide database as a tool for research and education. Nucleic Acids Res *44*, D1087–D1093. https://doi.org/10.1093/nar/gkv1278.

42. Pirtskhalava, M., Amstrong, A.A., Grigolava, M., Chubinidze, M., Alimbarashvili, E., Vishnepolsky, B., Gabrielian, A., Rosenthal, A., Hurt, D.E., and Tartakovsky, M. (2021). DBAASP v3: database of antimicrobial/cytotoxic activity and structure of peptides as a resource for development of new therapeutics. Nucleic Acids Res *49*, D288–D297. https://doi.org/10.1093/nar/gkaa991.

43. Shi, G., Kang, X., Dong, F., Liu, Y., Zhu, N., Hu, Y., Xu, H., Lao, X., and Zheng, H. (2022). DRAMP 3.0: an enhanced comprehensive data repository of antimicrobial peptides. Nucleic Acids Res *50*, D488–D496. https://doi.org/10.1093/nar/gkab651.

44. Agrawal, P., Bhalla, S., Usmani, S.S., Singh, S., Chaudhary, K., Raghava, G.P.S., and Gautam, A. (2016). CPPsite 2.0: a repository of experimentally validated cell-penetrating peptides. Nucleic Acids Res *44*, D1098–D1103. https://doi.org/10.1093/nar/gkv1266.

45. Wei, L., Tang, J., and Zou, Q. (2017). SkipCPP-Pred: an improved and promising sequence-based predictor for predicting cell-penetrating peptides. BMC Genomics *18*, 742. https://doi.org/10.1186/s12864-017-4128-1.

46. Manavalan, B., Subramaniyam, S., Shin, T.H., Kim, M.O., and Lee, G. (2018). Machine-Learning-Based Prediction of Cell-Penetrating Peptides and Their Uptake Efficiency with Improved Accuracy. J Proteome Res *17*, 2715–2726. https://doi.org/10.1021/acs.jproteome.8b00148.

47. Singh, S., Chaudhary, K., Dhanda, S.K., Bhalla, S., Usmani, S.S., Gautam, A., Tuknait, A., Agrawal, P., Mathur, D., and Raghava, G.P.S. (2016). SATPdb: a database of structurally annotated therapeutic peptides. Nucleic Acids Res *44*, D1119–D1126. https://doi.org/10.1093/nar/gkv1114.

48. Boukamp, P., Petrussevska, R.T., Breitkreutz, D., Hornung, J., Markham, A., and Fusenig, N.E. (1988). Normal keratinization in a spontaneously immortalized aneuploid human keratinocyte cell line. J Cell Biol *106*, 761–771. https://doi.org/10.1083/jcb.106.3.761.

49. Wan, F., Torres, M.D.T., Peng, J., and de la Fuente-Nunez, C. (2024). Deep-learning-enabled antibiotic discovery through molecular de-extinction. Nat Biomed Eng *8*, 854–871. https://doi.org/10.1038/s41551-024-01201-x.

50. CPPsite 2.0 http://crdd.osdd.net/raghava/cppsite/.

51. Shengjia Zhao, Jiaming Song, and Stefano Ermon (2018). InfoVAE: Information Maximizing Variational Autoencoders. https://doi.org/https://doi.org/10.48550/arXiv.1706.02262.

52. Kawashima, S. (2000). AAindex: Amino Acid index database. Nucleic Acids Res *28*, 374–374. https://doi.org/10.1093/nar/28.1.374.

53. Cesaro, A., Gaglione, R., Chino, M., De Luca, M., Di Girolamo, R., Lombardi, A., Filosa, R., and Arciello, A. (2022). Novel Retro-Inverso Peptide Antibiotic Efficiently Released by a Responsive Hydrogel-Based System. Biomedicines *10*, 1301. https://doi.org/10.3390/biomedicines10061301.

Figures

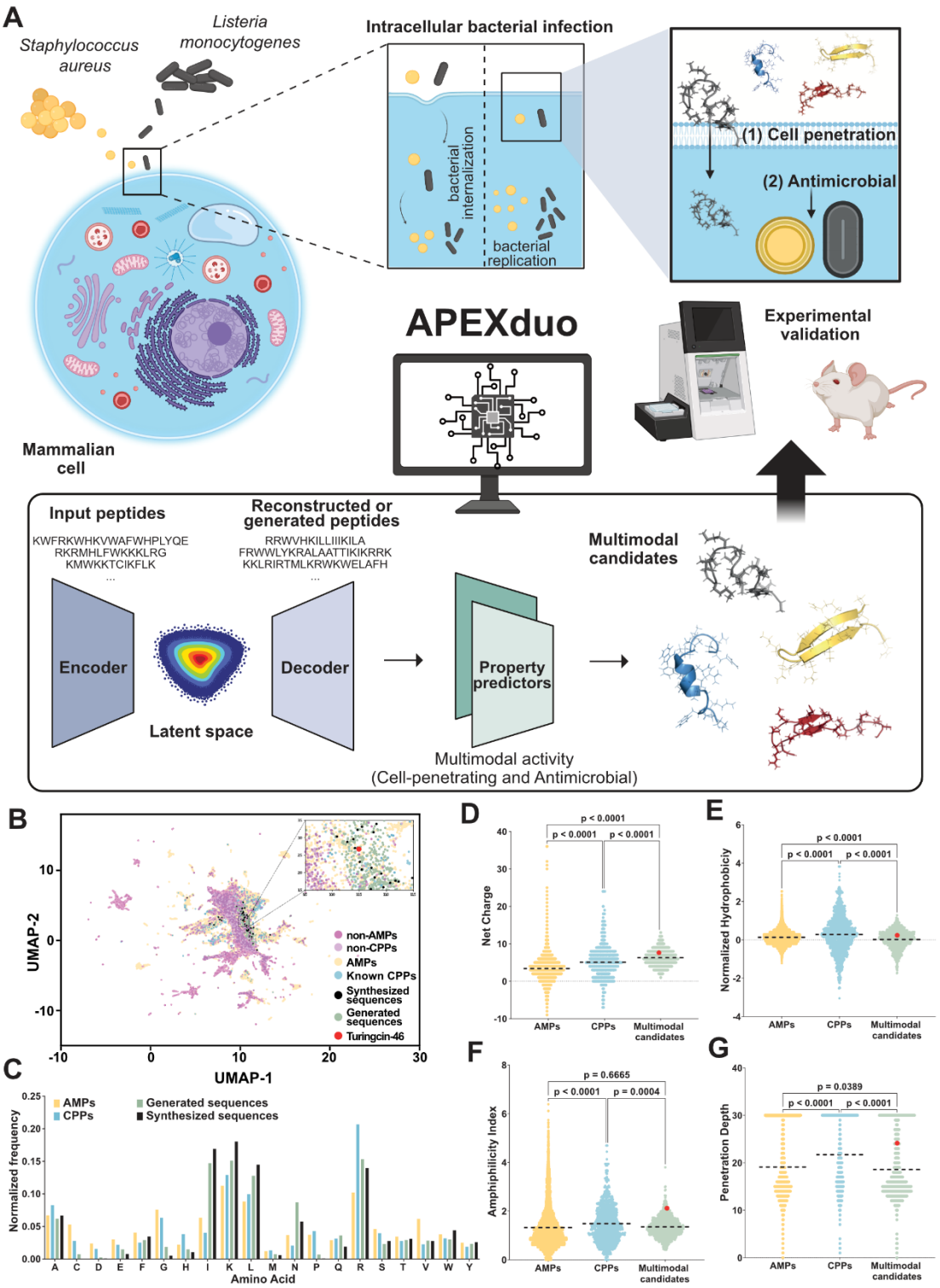

Figure 1. Multimodal peptide generation using deep learning. (A) A deep learning workflow capable of generating peptide candidates that can penetrate eukaryotic cells and eliminate intracellular *S. aureus* and *L. monocytogenes.* A variational autoencoder (VAE) was used to generate novel peptide sequences. The resulting candidates were then filtered using predictive deep learning models to select those with high antimicrobial and cell-penetrating potentials for further experimental validation. The peptide structures shown were rendered using the PyMOL Molecular Graphics System (version 3.0, Schrödinger, LLC). Figure created with BioRender.com. **(B)** Distribution of different peptide classes

in ESM2-derived sequence space. Sequences from publicly available AMPs and CPPs, as well as multimodal candidates generated by ApexDuo, were embedded into a 2D space after dimensionality reduction via a sequence similarity matrix. This analysis reveals that the newly generated multimodal candidates occupy a region distinct from non-AMP/CPP sequences, yet overlap with the known AMP/CPP space, suggesting the potential for dual functionality. **(C)** Comparison of amino acid frequencies in Turingcins (both generated and synthesized) against publicly available AMPs and CPPs. The multimodal peptides show a unique compositional profile, including a relative enrichment of lysine, isoleucine, leucine, and asparagine residues. **(D–G)** Comparative analysis of physicochemical properties among the multimodal candidates, AMPs, and CPPs. Properties include **(D)** net charge, **(E)** normalized hydrophobicity, **(F)** amphiphilicity index, and **(G)** penetration depth. Normalized hydrophobicity influences peptide-membrane interactions, net charge modulates electrostatic attractions with negatively charged bacterial membranes, amphiphilicity index correlates with the peptide's mechanism of membrane engagement, and penetration depth reflects how deeply the peptide integrates into lipid bilayers. All physicochemical properties of the peptides were obtained using the DBAASP server [39], and the hydrophobicity scale used was the Eisenberg and Weiss scale. Turingcin-46, the most promising multimodal candidate identified in this study, is indicated with a red dot. For panels **D–G**, statistical significance was determined via two-tailed t-tests followed by Mann–Whitney tests; p values are shown on the graphs. The dashed line within each distribution denotes the mean for that group.

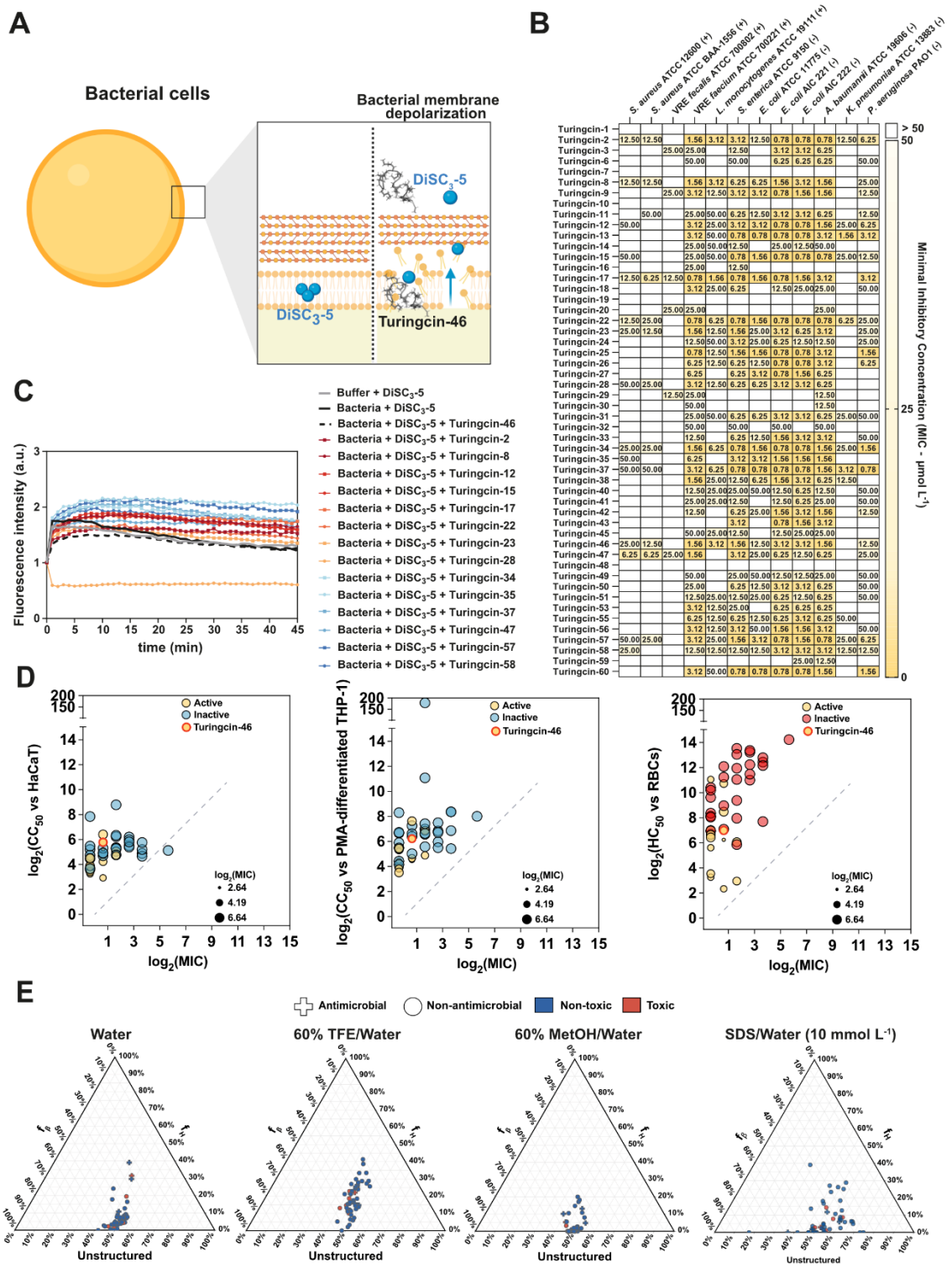

Figure 2. Antimicrobial activity, cytotoxicity, and secondary structure profiles of Turingcins. (A) Schematic overview of how Turingcins exert antimicrobial activity against *S. aureus*, including the induction of membrane depolarization. **(B)** Heat map showing the minimal inhibitory concentration (MIC) values of active Turingcins generated by ApexDuo against clinically significant Gram-positive (+) and Gram-negative (-) bacterial strains, including antibiotic-resistant isolates. Cells were treated with serial dilutions of each peptide (0.78–50 µmol L^{-1}) at 37 °C, and bacterial growth was measured after 24 hours via optical density at 600 nm. MIC values indicate the lowest concentration that completely inhibited growth, reported as the mode of two independent

679 replicates. **(C)** Relative fluorescence changes of *S. aureus* membranes treated with
680 Turingcins in the presence of the voltage-sensitive dye $DiSC_3$-5, indicating peptide-
681 induced membrane depolarization. All experiments were performed in three independent
682 replicates (see also **Figure S2A**) **(D)** Scatterplots correlating antimicrobial activity
683 (lowest MIC observed across all tested pathogens) with cytotoxicity [CC_{50} for human
684 keratinocytes (HaCaT), PMA-differentiated human monocytes (THP-1), and HC_{50} for
685 human red blood cells (RBCs)]. CC_{50} and HC_{50} values were derived from dose-response
686 curves obtained via non-linear regression analysis (see also **Figures S2B**, **C**, and **D**). The
687 dashed diagonal line (y = x) represents values of CC_{50} equals to MIC. Data points in
688 yellow indicate antimicrobial activity against *S. aureus* ATCC 12600, with point size
689 corresponding to the $\log_2$MIC against this strain. **(E)** Ternary plots depicting the
690 secondary structure composition (α-helix, β-sheet, and disordered) of each peptide at 50
691 μmol L^{-1} in different solvents: water, 60% trifluoroethanol (TFE) in water, 60% methanol
692 (MeOH) in water, and sodium dodecyl sulfate (SDS, 10 mmol L^{-1}) in water. Secondary
693 structure fractions were estimated using the BeStSel server [21] (see also **Figure S3**). Figure
694 created with BioRender.com.

695

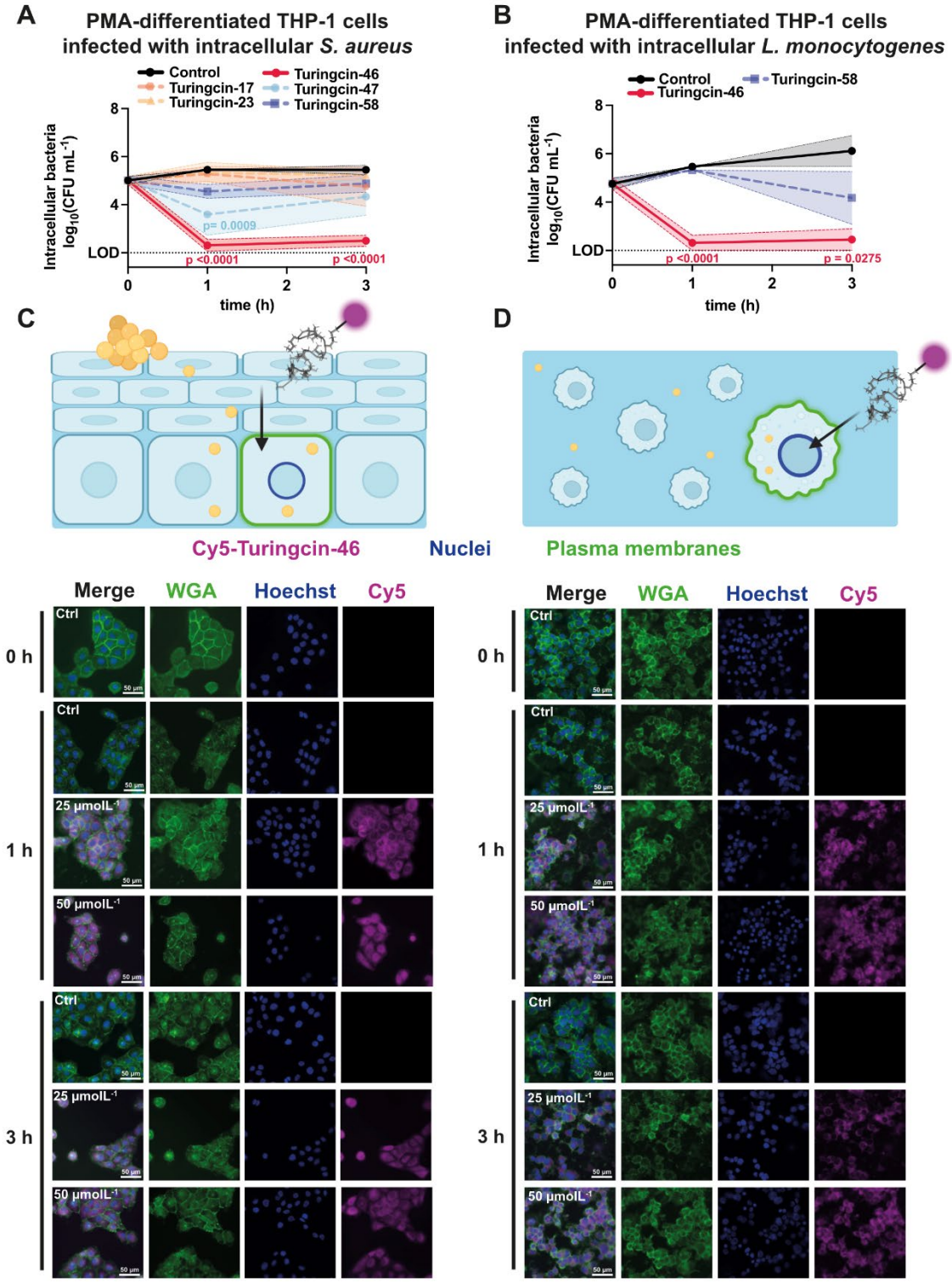

Figure 3. Intracellular antimicrobial activity of Turingcins. (A, B) Time-course analysis of the intracellular antimicrobial activity of Turingcin peptides at non-cytotoxic concentrations against *S. aureus* ATCC 12600 and *L. monocytogenes* ATCC 19111 in PMA-differentiated THP-1 macrophages. Intracellular bacterial loads were quantified at 0, 1, and 3 hours post-treatment (see also **Figure S6A-B** for extracellular bacteria counts). A minimum of two experiments was performed for all conditions, with the lead compound (Turingcin-46) tested in three replicates. **(C, D)** Representative fluorescence microscopy images of HaCaT and PMA-differentiated THP-1 cells treated with Cy5-labeled Turingcin-46, captured at 0-, 1-, and 3-hours post-treatment. Following peptide

706 incubation, samples were fixed with 4% PFA and stained with WGA 488 (10 μg mL^{-1})
707 to visualize plasma membranes and Hoechst 33342 (1 μg mL^{-1}) for nuclei visualization.
708 Each experiment was performed in biological duplicate, with two technical replicates
709 each. Figures were created using BioRender.com.
710

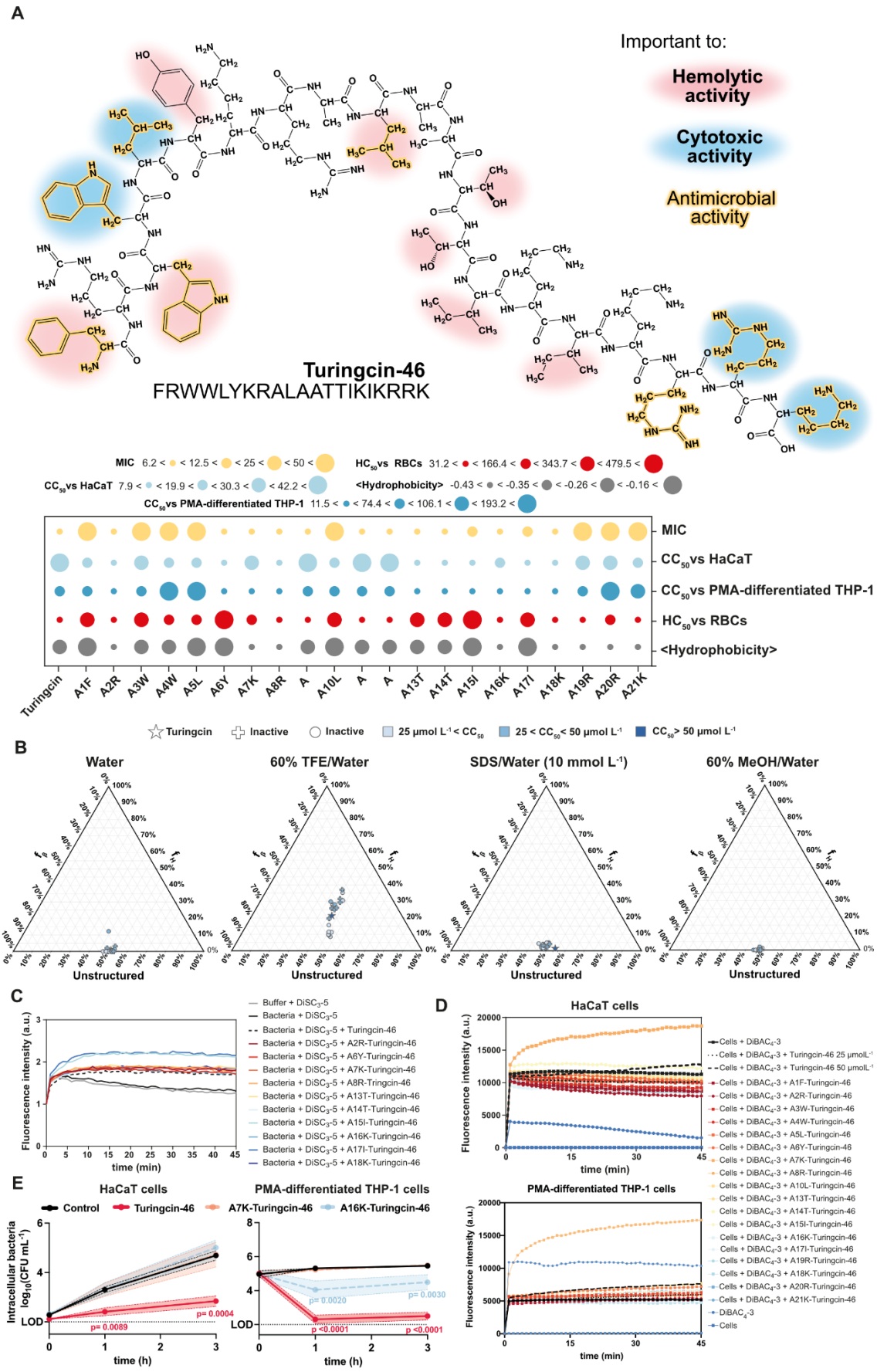
A
Important to:
Hemolytic activity
Cytotoxic activity
Antimicrobial activity
Turingcin-46
FRWWLYKRALAATTIKIKRRK
MIC
HC50 vs RBCs
CC50 vs HaCaT
<Hydrophobicity>
CC50 vs PMA-differentiated THP-1
Turingcin
Inactive
Inactive
25 μmol L-1 < CC50
25 < CC50 < 50 μmol L-1
CC50 > 50 μmol L-1
B
Water
60% TFE/Water
SDS/Water (10 mmol L-1)
60% MeOH/Water
Unstructured
C
Fluorescence intensity (a.u.)
time (min)
D
HaCaT cells
PMA-differentiated THP-1 cells
E
Control
Turingcin-46
A7K-Turingcin-46
A16K-Turingcin-46
Intracellular bacteria log10(CFU mL-1)
LOD
time (h)

711

712 **Figure 4. Structural and functional elucidation of Turingcin-46. (A)** Chemical
713 structure of Turingcin-46, with residues influencing antimicrobial activity (yellow),
714 cytotoxicity (blue), and hemolytic effects (red) highlighted. MIC (against *S. aureus*
715 ATCC 12600), CC_{50} (against HaCaT keratinocytes and PMA-differentiated THP-1
716 macrophages), HC_{50}, and normalized hydrophobicity values are presented in a bubble plot
717 to compare the wild-type Turingcin-46 sequence with 18 alanine-substituted variants (see
718 also **Figures S8A-D**). Normalized values (ranging from 0 to 1) were used for
719 visualization, while experimental data and normalized hydrophobicity values are
720 provided in the legend. The peptides hydrophobicity was obtained using the DBAASP
721 server [39] using the Eisenberg and Weiss scale. **(B)** Ternary plots showing the secondary
722 structure composition of each peptide (50 $\mu mol\ L^{-1}$) in different solvents: water, 60%
723 trifluoroethanol (TFE) in water, 60% methanol (MeOH) in water, and sodium dodecyl
724 sulfate (SDS, 10 $mmol\ L^{-1}$) in water. Secondary structures were estimated using the
725 BeStSel server [21] (see also **Figure S9A-E**). **(C)** Membrane depolarization of *S. aureus*
726 cells treated with Turingcin-46 and alanine-substituted derivatives that retained
727 antimicrobial activity. Changes in fluorescence intensity were measured using $DiSC_3$-5-
728 dye at MIC concentrations (see also **Figure S8E**). **(D)** Effects on eukaryotic cell
729 membrane potential (depicted as depolarization or hyperpolarization) for HaCaT and
730 PMA-differentiated THP-1 cells treated with Turingcin-46 and alanine variants,
731 evaluated using $DiBAC_4$-3 dye at CC_{50} concentrations (see also **Figures S8F-G**). **(E)**
732 Time-course analysis (0, 1, and 3 hours) of intracellular antimicrobial activity of
733 Turingcin-46, K7A-Turingcin-46, and K16A-Turingcin-46 at non-cytotoxic
734 concentrations against intracellular *S. aureus* in HaCaT keratinocytes and PMA-
735 differentiated THP-1 macrophages (see also **Figure S9F-G** for extracellular bacteria
736 counts). All experiments were carried out in three independent replicates.
737

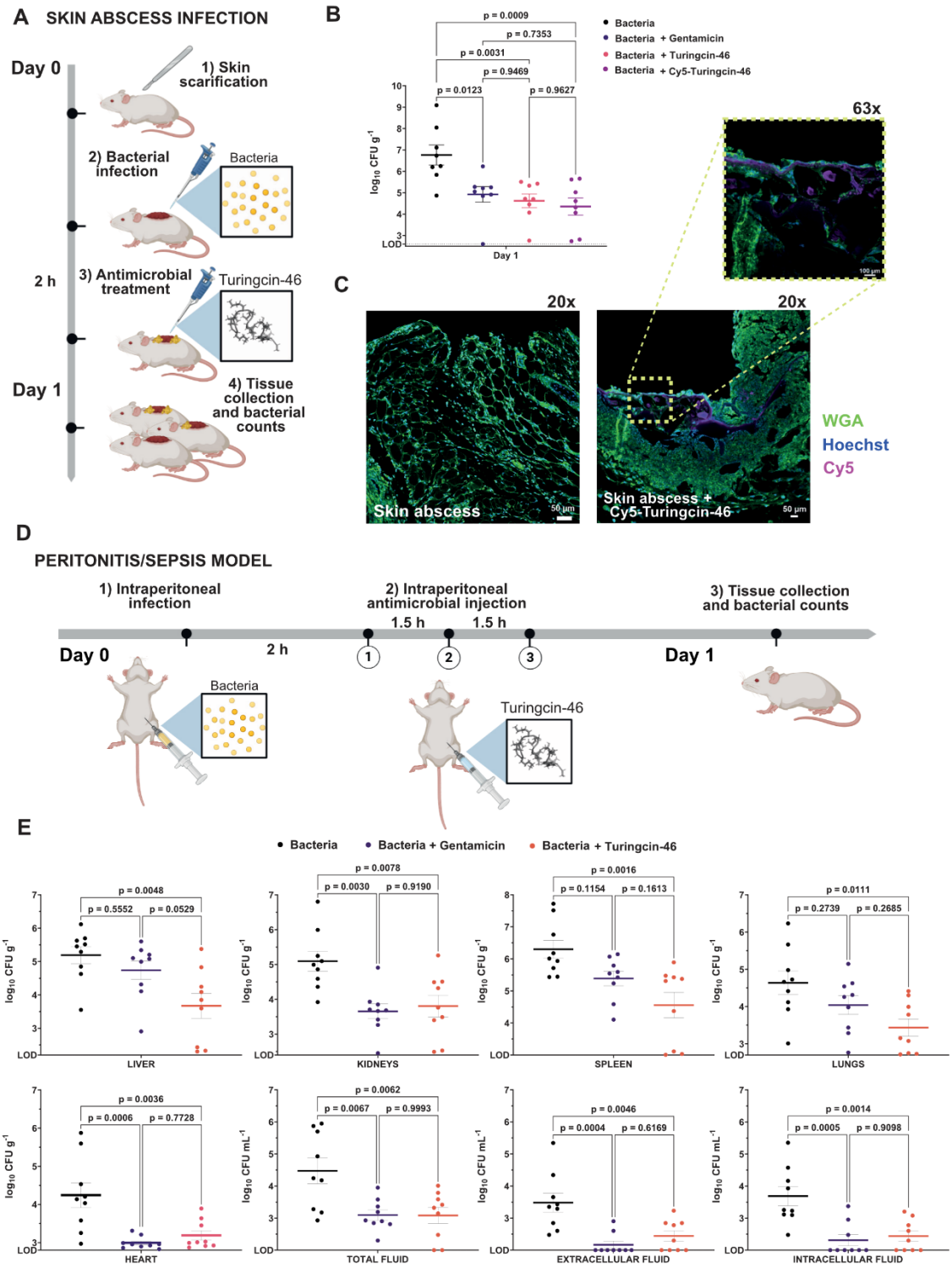

Figure 5. Anti-infective activity of Turingcin-46 in animal models. (A) Schematic representation of the skin abscess mouse model used to evaluate the anti-infective efficacy of Turingcin-46 against *S. aureus* ATCC 12600. **(B)** In the skin abscess model, a single post-infection administration of Turingcin-46 significantly reduced bacterial load compared to the untreated control. **(C)** Representative confocal laser scanning microscopy (CLSM) images of excised skin tissues from untreated mice and those treated with Cy5-Turingcin-46. Deparaffinized tissue sections were stained with WGA 488 (10 μg mL^{-1}) to visualize plasma membranes and Hoechst 33342 (1 μg mL^{-1}) for nuclei. **(D)** Schematic representation of the peritonitis/sepsis mouse model, in which Turingcin-46

was administered intraperitoneally. **(E)** Anti-infective efficacy against *S. aureus* ATCC 12600 was evaluated one day after injection of Turingcin-46, demonstrating significant efficacy in in multiple organs (liver, kidneys, spleen, lungs, heart) and peritoneal fluids (total, extracellular, intracellular - see also **Figure S11** for correlations between intracellular and extracellular *S. aureus* CFU counts in peritoneal lavage samples). Compared to the untreated control, Turingcin-46 treatment significantly decreased bacterial loads. Statistical significance in **(B, E)** was determined using one-way ANOVA followed by Tukey's test; p values are shown in the graphs. The solid line within each distribution represents the mean. Panels **(A)** and **(D)** were created with BioRender.com.

Data and code availability

All public databases used for building ApexDuo are listed in the key resources table. Pretrained models for ApexDuo are available on Gitlab (https://gitlab.com/machine-biology-group-public/apex_duo) and listed in the key resources table. Any additional information needed to reanalyze the data presented in this paper can be obtained from the lead contact upon request.

Methods

Datasets

Peptides used for training the deep generative model were curated from UniRef50 [40]. We filtered out protein sequences having more than 50 amino acids. The peptides we downloaded from UniRef50 were divided into a training set and a validation set with 1,418,011 and 354,503 peptides, respectively. AMPs used for updating antimicrobial predictor APEX consists of two parts. One part is the DBAASP [39] dataset used in the original APEX work [49], which contained 14,738 measured antimicrobial activities (MICs) values for 988 peptides against 34 bacterial strains. The other part is our updated in-house antimicrobial activity dataset with 1,016 peptides, 37 strains (three new strains including *Porphyromoras gingivalis* ATCC BAA-308, *Neisseria meningitis* ATCC 13077, and *E. coli* K1 ATCC 700973) and 14,963 MIC values. Public AMPs used for computational analysis were retreived from public databases, including APD3 [41], DBAASP [42] and DRAMP [43], as well as our in-house peptides having minimum inhibitory concentration ≤128 μmol L^{-1} against at least one bacterial strain [49]. CPPs used for training and computational analysis were retreived from CPPsite 2.0 [44,50], SkipCPP-Pred [45] and MLCPP [46]. We also curated toxic peptides from SATPdb [47] and labeled them as negative data so that the CPP predictor can balance the cell-penetrating property and toxicity and help to retrieve peptides with good cell penetration and relatively low toxicity. After cleaning the non-canonical peptides and removing duplicates, we obtained 1,217 CPPs and 5,293 non-CPPs or toxic peptides for CPP predictor building.

Variational autoencoder

We use a maximum mean discrepancy variational autoencoder (MMD-VAE) as our peptide sequence generator [51]. The MMD-VAE consists of an encoder $E(\cdot)$ and a decoder $D(\cdot)$, both typically implemented as neural networks. The encoder and decoder form a compression and de-compression process that enables representation learning, distribution learning and novel data generation. In our scenario, the inputs to the encoder

are peptide sequences. For a peptide sequence with l amino acids, two special characters indicating the start and end of the sequence are added at the beginning and end, respectively. One-hot encoding is then used to numerically represent this sequence. Let x denotes this representation, the encoder takes x and generates a continuous vector (i.e., a latent code) $v = E(x) \in \mathbb{R}^d$, where d stands for the dimension of v. The decoder uses the latent code v to generate a peptide sample $x' = D(v)$ that resembles x. Given a peptide set to train the MMD-VAE and let $p_{data}(x)$ denote the empirical distribution of training peptides, the minimization goal of MMD-VAE can be written as

$$loss = -\mathbb{E}_{p_{data}(x)}\left[\mathbb{E}_{p(v|x)}[\log p(x|v)]\right] + \mathrm{MMD}(p(v|x), p_{prior}(v)) \qquad \text{Eq.1}$$

where $\mathbb{E}[\cdot]$ stands expectation, $p(v|x)$ is the posterior distribution of the latent codes given xs from $p_{data}(x)$, MMD is the maximum mean discrepancy that measures the distance of two probability distributions, and $p_{prior}(v)$ is the prior distribution of v. In our case, the log-likelihood $\log p(x|v)$ in Eq.1 is equal to the negative cross entropy between x from $p_{data}(x)$ and its reconstructed version by $D\big(E(x)\big)$ the MMD-VAE. In this sense, Eq.1 can be re-written as

$$loss = \mathbb{E}_{p_{data}(x)}\,[\mathrm{CE}(x, D(E(x))] + \mathrm{MMD}(p(v|x), p_{prior}(v)),$$

where $\mathrm{CE}(\cdot,\cdot)$ is the cross entropy. Optimizing the parameters of $E(\cdot)$ and $D(\cdot)$ to minimize $\mathbb{E}_{p_{data}(x)}\,[\mathrm{CE}(x, D(E(x))]$ ensures the MMD-VAE to capture the distribution of training peptide sequences (hence, the decoder can generate peptides resemble the training ones) while the optimization of $E(\cdot)$ and $D(\cdot)$ for $\mathrm{MMD}(p(v|x), p_{prior}(v))$ makes the latent codes vs close to the prior distribution (hence, making it easier for the users to sample latent codes from the prior distribution and generate new peptide samples). In our practice, the prior distribution is the zero-mean, unit-variance multivariate Gaussian distribution. The encoder begins by mapping the one-hot encoding of a peptide to a learnable embedding layer $\boldsymbol{x} \in \mathbb{R}^{L\times e}$, where L stands for the input length and e denotes the feature dimension. Then the encoder uses a recurrent neural network (implemented as gated recurrent units) to map $\boldsymbol{x}$ to hidden features $\boldsymbol{h} \in \mathbb{R}^{L\times k}$, where k denotes the number of hidden units. We then adopt an attention mechanism to fuse contextual residue information by

$$\boldsymbol{att1} = \mathbf{Softmax}(\mathbf{Linear}_{\mathbf{att1}}\big(\mathbf{concat}(\boldsymbol{h}, \boldsymbol{x})\big)) \in \mathbb{R}^{L\times L},$$

$$\boldsymbol{h_{fused}} = \boldsymbol{att1} \times \boldsymbol{h} \in \mathbb{R}^{L\times k},$$

where $\mathbf{Linear}_{\mathbf{att1}}(\cdot)$ is a linear transformation, $\mathbf{concat}(\cdot,\cdot)$ is concatenation operation along the feature dimension (i.e., the last dimension), $\mathbf{Softmax}(\cdot)$ is the softmax function and also applied to the last dimension of its input. After that, we use another attention mechanism to final latent code $\boldsymbol{h_{latent}}$ of the peptide by

$$\boldsymbol{att2} = \mathbf{Softmax}(\mathbf{Linear}_{\mathbf{att2}}\big(\boldsymbol{h_{fused}}\big)) \in \mathbb{R}^{L\times 1},$$

$$\boldsymbol{h_{peptide}} = \boldsymbol{att2}^{\mathbf{T}} \times \boldsymbol{h_{fused}} \in \mathbb{R}^{1\times k},$$

$$\boldsymbol{h_{latent}} = \mathbf{Linear}_{\mathbf{latent}}(\boldsymbol{h_{peptide}}) \in \mathbb{R}^{1\times d}.$$

The decoder is a recurrent neural network with the same architecture as that from the encoder followed by a fully-connected neural network layer to transform the latent code to the residue type probabilities per amino acid position. We used a learning rate of 0.0001 to train the MMD-VAE 1,000 epochs on the training set. The number of recurrent neural network layers, the number of hidden units in the recurrent neural network, the dimension of the latent code, batch size, weight decay strength, and the best epoch were chosen by the $loss$ of the trained model evaluated on the validation set.

Peptide generation

Instead of directly sampling latent codes to generate peptide samples, we followed the previous practice to fit a kernel density estimator (KDE) to the functional peptides. That is, we obtained the latent codes of our in-house peptides and publicly available CPPs. A KDE (implemented by scikit-learn with default hyperparameter) was used to fit the distribution of these latent codes. We then sampled the latent codes from the KDE and decoded the sampled codes by the decoder to obtain the generated peptide sequences. We sampled 50M latent codes and generated the corresponding sequences for further filtering by the antimicrobial and cell-penetrating peptide predictors.

Antimicrobial peptide predictor

The antimicrobial peptide predictor we used is APEX [49], a multi-bacterial multi-strain antimicrobial peptide predictor previously been built for mining antibiotic encrypted peptides from proteomes of extinct organism. APEX uses the same architecture of the encoder of our variational autoencoder except we drop the embedding layer and use AAindex[52] descriptors of amino acid sequences as inputs. That is, given an input peptide, it is represented as $\boldsymbol{x} \in \mathbb{R}^{L\times 566}$, where L is peptide length and ith column of $\boldsymbol{x}$ is a 566-dimensional vector storing the physicochemical and biochemical properties of ith amino acid in the peptide. After extracting the $\boldsymbol{h_{latent}}$, we apply multilayer perceptron to process $\boldsymbol{h_{latent}}$ and predict antimicrobial peptides. For each generated peptide, we used APEX to obtain the median value of predicted minimum inhibitory concentrations (MICs) against multiple bacterial strains.

Cell-penetrating peptide predictor

We used deep learning to build the binary classifier to predict the cell-penetrating property of peptide sequences. Our predictor has similar architecture to that of the encoder of MMD-VAE except that we added one more fully-connected neural network layer to the hidden peptide features to the cell-penetrating probabilities. We set the learning rate = 0. 0001, batch size = 128, the number of training epochs = 100, and trained each model five times under different seeds to create an ensemble version of it (i.e., we averaged the prediction result from each model). Hyperparameters (i.e., the number of recurrent neural network layers, the hidden unit size, and weight decay strength) of the CPP predictor were selected based on the mean of the area under the receiver operating characteristic under the five-fold cross validation. The CPP predictors from the top five hyperparameter

873 combinations were selected (i.e., 25 models = 5 hyperparameter combinations × 5 copies
874 under different random seeds) for the CPP peptide screening.

875

876 **Peptide selection**

877 We used the following rules to filter and select the desired peptides from 50M generated
878 peptides from the MMD-VAE.

879 (1) Generated peptides having median MIC >32 μmol L^{-1} were filtered out from
880 our selection.
881 (2) After screening the CPP probabilities for the 50M generated peptides, we
882 calculated the mean and standard deviation of the predicted probabilities
883 among the 50M sequences. Generated peptides passing 3-sigma rule (i.e., CPP
884 prediction ≥ mean of CPP prediction + 3 × standard deviation of CPP
885 prediction) were kept.
886 (3) Generated peptides having more than 30 amino acid residues were filtered out
887 due to synthesis difficulty.

888 (4) Generated peptides appeared in our in-house peptide data or training CPPs
889 were removed.

890 (5) Remaining generated peptides were ranked by median MIC, and we used
891 Striped Smith–Waterman algorithm to perform pair-wise sequence alignment
892 and calculate the sequence similarity between two peptides. We kept the
893 peptide with lower median MIC when a pair of peptides having a sequence
894 similarity > 0.5.

895

896 **Physicochemical properties extraction**

897 The twelve physicochemical properties of the peptides, including normalized
898 hydrophobic moment, normalized hydrophobicity, net charge, amphiphilicity index,
899 isoelectric point, penetration depth, tilt angle, disordered conformation propensity, linear
900 moment, tendency for in vitro aggregation, angle between hydrophobic residues, and
901 propensity for PPII coil, were obtained using the DBAASP server [39]. The hydrophobicity
902 scale used was the Eisenberg and Weiss scale.

903

904 **Peptide synthesis**

905 The peptides used in the experiments were procured from AAPPTec and produced
906 through solid-phase synthesis employing the Fmoc strategy.

907

908 **Bacterial strains and growth conditions**

909 In this study, we worked with the following pathogenic bacterial strains: *Staphylococcus*
910 *aureus* ATCC 12600, *Staphylococcus aureus* ATCC BAA-1556 (methicillin-resistant
911 strain), *Enterococcus faecalis* ATCC 700802 (vancomycin-resistant strain),
912 *Enterococcus faecium* ATCC 700221 (vancomycin-resistant strain), *Listeria*
913 *monocytogenes* ATCC 19111, *Salmonella enterica* ATCC 9150, *Escherichia coli* ATCC

914 11775, *Escherichia coli* AIC221 [*Escherichia coli* MG1655 phnE_2::FRT (control strain
915 for AIC222)], *Escherichia coli* AIC222 [*Escherichia coli* MG1655 pmrA53
916 phnE_2::FRT (polymyxin resistant; colistin-resistant strain)], *Acinetobacter baumannii*
917 ATCC 19606, *Klebsiella pneumoniae* ATCC 13883, and *Pseudomonas aeruginosa*
918 PAO1. All strains were cultured in Luria-Bertani (LB) broth or on LB agar, except for *L.*
919 *monocytogenes*, which was cultured in Brain Heart Infusion (BHI) medium, and *S.*
920 *aureus*, which was grown on mannitol salt agar plates. Bacterial cultures for all
921 experiments were started from a single isolated colony and grown overnight (16 hours)
922 in liquid medium at 37 °C. The next day, the cultures were diluted 1:100 into fresh
923 medium and incubated at 37 °C until reaching the mid-logarithmic growth phase.

924

925 **Minimal inhibitory concentration assays**

926 Broth microdilution assays were conducted to determine the MIC, the minimum
927 inhibitory concentration required to achieve complete bacterial elimination, for each
928 peptide. Peptides were prepared in sterile water and serially diluted twofold in untreated
929 polystyrene 96-well plates, with final concentrations ranging from 0 to 100 µmol L^{-1}, as
930 previously described[11,53]. Bacterial cultures, adjusted to 4×10^6 CFU mL^{-1} in LB or BHI
931 medium, were combined with the peptide solutions in equal volumes. After 24 hours of
932 incubation at 37 °C, absorbance at 600 nm was measured using a spectrophotometer. The
933 MIC was identified as the lowest peptide concentration that prevented visible bacterial
934 growth. Negative control wells without peptide were included to confirm uninhibited
935 bacterial growth.

936

937 **Bacterial membrane depolarization assays using $DiSC_3$-5**

938 A cytoplasmic membrane depolarization assay was carried out using the membrane
939 potential-sensitive dye 3,3'-dipropylthiadicarbocyanine iodide ($DiSC_3$-5, Sigma 43608).
940 Mid-logarithmic phase *S. aureus* ATCC 12600 was washed and adjusted to an optical
941 density of 0.05 at 600 nm in HEPES buffer (pH 7.2) supplemented with 20 mmol L^{-1}
942 glucose and 0.1 mol L^{-1} KCl. The bacterial suspension (100 µL per well) was incubated
943 with 10 µmol L^{-1} $DiSC_3$-5 for 15 minutes. This allowed fluorescence to stabilize as the
944 dye incorporated into the bacterial membrane. The peptides were subsequently added at
945 concentrations corresponding to their MIC values in a 1:1 ratio with the bacterial
946 suspension. Fluorescence changes (λ_{ex} = 622 nm, λ_{em} = 670 nm) were recorded over 45
947 minutes to monitor membrane depolarization.

948

949 **Eukaryotic cell culture conditions**

950 Immortalized human keratinocytes (HaCaT, sourced from Deutsches
951 Krebsforschungszentrum - DKFZ [48]) and human monocytes (THP-1, ATCC TIB-202)
952 were maintained in high-glucose Dulbecco's modified Eagle's medium (DMEM) and
953 Roswell Park Memorial Institute 1640 (RPMI), respectively. Both media were enriched
954 with 1% antibiotics (penicillin/streptomycin) and 10% fetal bovine serum (FBS). The
955 cells were cultured at 37 °C in a humidified incubator with 5% CO_2.

956

957 **Cytotoxicity assays**

958 For HaCaT cells, 5×10^3 cells per well were seeded into 96-well plates one day prior to
959 treatment with increasing peptide concentrations (3.12–50 μmol L^{-1}). THP-1 monocytes
960 were differentiated into macrophages by treating them with 100 nmol L^{-1} phorbol 12-
961 myristate 13-acetate (PMA) for three days before administering the peptides. After a 24-
962 hour incubation with each peptide, an MTT assay was performed. Briefly, MTT reagent
963 (0.5 mg mL^{-1}) in phenol red-free medium (DMEM for HaCaT cells and RPMI for PMA-
964 differentiated THP-1 cells) was added to each well (100 μL per well). The plates were
965 incubated at 37 °C for 4 hours to facilitate the formation of insoluble formazan salts.
966 These salts were subsequently dissolved in a solution of 0.04 mol L^{-1} hydrochloric acid
967 (HCl) in anhydrous isopropanol, and the absorbance at 570 nm was recorded using a
968 spectrophotometer.

969

970 **Hemolysis assays**

971 To assess the release of hemoglobin from human red blood cells (RBCs) following
972 treatment with each peptide, human erythrocytes (blood type A-, obtained from ZenBio,
973 using heparin-anticoagulated blood) were washed three times with PBS (pH 7.4) by
974 centrifugation at 800 g for 10 minutes. A 1:200 dilution of RBCs (75 μL) was combined
975 with different concentrations of peptide solution (0.78–100 μmol L^{-1}; 75 μL), and the
976 resulting mixture was incubated at room temperature for 4 hours. After incubation, the
977 mixture was centrifuged at 1,300 g for 10 minutes to pellet the cells and debris. The
978 supernatant (100 μL) from each well was moved to a new 96-well plate for absorbance
979 analysis at 405 nm using an automated plate reader. The percentage of hemolysis was
980 calculated by comparing the absorbance to the negative control (PBS) and the positive
981 control (1% SDS in PBS, v/v).

982 $$Hemolysis\ (\%) = \frac{100 \times (Absorbance_{405\ nm\ peptide} - Absorbance_{405\ nm\ negative\ control})}{(Absorbance_{405\ nm\ positive\ control} - Absorbance_{405\ nm\ negative\ control})}$$

983

984 **Circular dichroism experiments**

985 Circular dichroism (CD) measurements were performed using a J1500 CD
986 spectropolarimeter (Jasco) at the Biological Chemistry Resource Center (BCRC) of the
987 University of Pennsylvania. The experiments were carried out at 25 °C, and the spectra
988 shown are the result of averaging three accumulations. A quartz cuvette with a 1.0 mm
989 optical path length was used, covering a wavelength range of 260–190 nm at a scanning
990 speed of 50 nm min^{-1} and a bandwidth of 0.5 nm. Peptide samples were tested at a
991 concentration of 50 μmol L^{-1} in various environments: water, a 60% trifluoroethanol
992 (TFE) in water mixture, a 50% methanol (MeOH) in water mixture, and water containing
993 sodium dodecyl sulfate (SDS) at 10 mmol L^{-1}. Baseline readings were taken before data
994 acquisition, and a Fourier transform filter was used to minimize background noise. The
995 secondary structure fraction values were calculated using the single-spectrum analysis
996 tool on the BeStSel server [21]. Ternary plots were created in https://www.ternaryplot.com/
997 and subsequently edited.

998

999 **Intracellular antimicrobial activity**

1000 HaCaT and PMA-differentiated THP-1 cells were seeded at a density of 50,000 cells per
1001 well (100 µL) in antibiotic-free medium. Cells were incubated for 2 hours with *S. aureus*
1002 ATCC 12600 or *L. monocytogenes* to allow infection, using initial bacterial densities of
1003 0.002 or 0.01 OD_{600} mL^{-1} for keratinocytes, and 0.001 or 0.002 OD_{600} mL^{-1} for
1004 macrophages, respectively. After the incubation period, gentamicin was added at a final
1005 concentration of 500 µg mL^{-1} to remove extracellular bacteria. Following gentamicin
1006 removal, samples were treated with peptides at concentrations of 12.5, 25, and 50
1007 µmol mL^{-1} or with gentamicin (as a negative control) at 5, 100, and 500 µg mL^{-1}. At
1008 designated time points (0, 1, and 3 hours post-treatment), the supernatants were collected,
1009 serially diluted 10-fold, and plated on LB agar for colony counting. The cellular pellets
1010 were washed with PBS, lysed using 1% Triton X-100, and similarly plated on LB agar
1011 for bacterial enumeration.

1012

1013 **Fluorescence microscopy analysis of Cy5-Turingcin-46 internalization in eukaryotic**
1014 **Cells**

1015 HaCaT and PMA-differentiated THP-1 cells were seeded on glass coverslips in 24-well
1016 plates at densities of 50,000 and 400,000 cells per well, respectively. Experimental
1017 conditions were designed to evaluate Cy5-Turingcin-46 internalization in both infected
1018 and uninfected cells. For the infection condition, cells were incubated for 2 hours with *S.*
1019 *aureus* ATCC 12600 at an initial bacterial density of 0.02 OD mL^{-1} to enhance bacterial
1020 visualization under the microscope. Following bacterial exposure, cells were treated with
1021 gentamicin for an additional 2 hours as previously described. After treatment, cells were
1022 washed with PBS and incubated with Cy5-Turingcin-46 or Cy5 alone at concentrations
1023 of 25 and 50 µmol L^{-1}. In parallel, In parallel, treatments with peptide or Cy5 alone were
1024 performed on uninfected cells that were not exposed to *S. aureus*. At three time points (0,
1025 1, and 3 hours post-treatment), cells were washed with PBS and fixed with 4%
1026 paraformaldehyde in PBS for 15 minutes at room temperature. Nuclei, cell walls, and
1027 bacteria were stained using Hoechst 33342 (1 µg mL^{-1}) and wheat germ agglutinin
1028 conjugated to Alexa Fluor 488 (WGA 488, 10 µg mL^{-1}) for 20 minutes at room
1029 temperature. The stained cells were washed twice with PBS, mounted on glass slides, and
1030 imaged using a Nikon fluorescence microscope.

1031

1032 **Eukaryotic membrane depolarization assays using $DiBAC_4$-3**

1033 HaCaT and PMA-differentiated THP-1 cells were seeded at a density of 50,000 cells per
1034 well in 96-well plates (Corning 3904) using phenol red-free medium to minimize
1035 background fluorescence. Cellular monolayers were washed twice with 100 µL of a
1036 physiological buffer composed of 140 mmol L^{-1} NaCl, 5.4 mmol L^{-1} KCl, 1 mmol L^{-1}
1037 $CaCl_2$, 1 mmol L^{-1} $MgCl_2$, 10 mmol L^{-1} glucose, and 10 mmolL^{-1} HEPES (pH 7.4) to
1038 remove residual medium. The cells were subsequently incubated with 5 µmol L^{-1}
1039 $DiBAC_4$-3, a voltage-sensitive anionic dye (Thermo Fisher, catalog no. B438), prepared
1040 in the same buffer. This incubation was conducted at 37°C for 40 minutes to ensure
1041 adequate dye uptake and equilibration. Following incubation, the monolayers were gently
1042 washed to remove excess dye before being exposed to peptides at their CC_{50}
1043 concentrations. Fluorescence changes (λ_{ex} = 490 nm, λ_{em} = 516 nm) were recorded in real-

1044 time for 45 minutes using a microplate reader, providing a quantitative assessment of
1045 membrane depolarization dynamics.

1046

1047 **Resistance to proteolytic degradation assay**

1048 The stability of Turingcin-46 against enzymatic degradation was assessed by incubation
1049 in a solution containing 25% human serum in water. Specifically, the peptide, at a
1050 concentration of 7 mg mL^{-1}, was incubated with an aqueous solution of 25% human serum
1051 (Zen-Bio; healthy donor, blood type A-) at 37 °C for 6 hours. Samples were collected at
1052 0.5, 1, 2, 4, and 6 hours, and each aliquot was immediately treated with 10 µL of
1053 trifluoroacetic acid in ice for 10 minutes to halt enzymatic activity. Peptide analysis was
1054 performed using a Waters Acquity ultra-high-performance liquid chromatography-mass
1055 spectrometry (UHPLC-MS) system featuring a photodiode array detector (190–400 nm
1056 data collection) and a Waters single quadrupole detector 2 (SQD2). The setup included a
1057 Waters XBridge C_{18} column (3.5 µm, 4.6 mm x 50 mm), with a mobile phase consisting
1058 of 100% water containing 0.1% (v/v) formic acid (solvent A) and 100% acetonitrile
1059 (solvent B). Both solvents were of Fisher Optima grade. A 20 µL injection volume was
1060 used, and ionization was carried out in both positive and negative ESI modes, scanning a
1061 mass range of m/z 100–3,000. The gradient used consisted in 5-95% solvent B in 6 min.
1062 The proportion of intact peptide remaining at each time point was calculated by
1063 integrating the area under the curve of the peptide peak at the initial time (t = 0) as a
1064 reference. The experiments were done in three replicates.

1065

1066 **Skin abscess infection mouse model**

1067 Six-week-old female CD-1 mice were anesthetized, and their backs were shaved. The
1068 area was then wiped with ethanol to eliminate any endogenous S*taphylococci* prior to
1069 creating a surface abrasion using a scalpel. An aliquot of *S. aureus* ATCC 12600 (10^7
1070 CFU mL^{-1}; 20 µL), grown to an optical density of 0.45 at 600 nm in LB medium and
1071 washed twice with sterile PBS (pH 7.4) by centrifugation (5,000 g for 5 minutes), was
1072 applied to the scratched region. Peptide or gentamicin, each diluted to the $10\times MIC_{100}$,
1073 was administered to the wound site 2 hours post-infection. One day after the infection,
1074 the animals were euthanized, and the infected skin was excised. The tissues were weighed
1075 and processed into a homogenized mixture using a bead beater at 25 Hz for 20 minutes.
1076 The samples were then serially diluted 10-fold and plated on Mannitol Salt Agar (MSA)
1077 plates for colony-forming unit (CFU) quantification. Ten mice per group were included
1078 in the study, with two animals designated for histological analysis. All procedures were
1079 approved by the University Laboratory Animal Resources (ULAR) at the University of
1080 Pennsylvania (Protocol 806763).

1081

1082 **Peritonitis/sepsis mouse model**

1083 Six-week-old female CD-1 mice (stock number: 18679700-022) were infected
1084 intraperitoneally (I.P.) with *S. aureus* ATCC 12600 (5×10^{10} CFU mL^{-1}; 100 µL). The
1085 bacteria were cultured to an optical density of 0.5 at 600 nm in LB medium, washed twice
1086 with sterile PBS (pH 7.4) by centrifugation (3,500 g for 10 minutes), and resuspended in
1087 PBS. Mice were treated with three intraperitoneal doses of either gentamicin (460 µmol

1088 L^{-1}) or peptide (975 μmol L^{-1}), each administered in a 100 μL volume at 1.5-hour
1089 intervals, beginning 2 hours post-infection. Twenty-four hours after the final treatment,
1090 the mice were euthanized, and peritoneal fluids were collected by washing the peritoneal
1091 cavity with 5 mL of ice-cold PBS. The bacterial load in the fluids was assessed by
1092 dividing the sample into two equal fractions. For extracellular bacteria quantification, one
1093 fraction was centrifuged at 300 g for 10 minutes at 4 °C, and the supernatant was plated
1094 on MSA plates. For intracellular bacteria quantification, the second fraction was
1095 centrifuged at 1,000 rpm for 5 minutes at 4 °C, and the resulting pellet was treated with
1096 gentamicin (500 μg mL^{-1}) for 3 hours at 37 °C to eliminate extracellular bacteria. The
1097 pellet was then washed twice with PBS, serially diluted, and plated on MSA plates. Liver,
1098 kidneys, spleen, lungs, and heart were harvested, weighed, and homogenized using a bead
1099 beater (25 Hz for 20 minutes). The homogenates were plated on MSA to evaluate bacterial
1100 dissemination to these organs. Nine mice per group were included in the study. All
1101 procedures were approved by the University Laboratory Animal Resources (ULAR) at
1102 the University of Pennsylvania (Protocol 807530).

1103

1104 **Histological analysis**

1105 Skin tissues from mice, both untreated and treated with Cy5-Turingcin-46, were
1106 collected, fixed in 4% paraformaldehyde in PBS overnight at 4 °C, and stored in 70%
1107 ethanol prior to sectioning. Tissue sections were deparaffinized and rehydrated through a
1108 series of 5-minute incubations in xylene followed by a graded ethanol series (100% to
1109 70%).

1110 The slides were washed in PBS, and antigen retrieval was performed in citrate buffer (10
1111 mmol L^{-1} citrate, pH 6) at 90 °C for 1 hour. After antigen retrieval, the slides were washed
1112 again in PBS and blocked with 2% BSA and 0.05% Tween 20 in PBS for 30 minutes.
1113 Sections were then incubated with WGA 488 (10 μg mL^{-1}) in 2% BSA and 0.05% Tween
1114 20 in PBS for 30 minutes. Following this, the sections were washed twice in PBS for 3
1115 minutes each and stained with Hoechst 33342 (1 μg mL^{-1}) in PBS for 5 minutes. The
1116 sections were then washed twice in PBS for 3 minutes each and mounted using a
1117 mounting medium. Images were acquired using Zeiss LSM 980 confocal maintained by
1118 the CDB Microscopy Core.

1119

1120 **Quantification and statistical analysis**

1121 **Reproducibility of the experimental assays**

1122 Unless specified otherwise, all assays were performed in three independent biological
1123 replicates, as outlined in the figure legends and the Experimental Models and Methods
1124 sections. Cytotoxic and hemolytic activity values were calculated using non-linear
1125 regression analysis of peptide screenings across a concentration gradient, representing the
1126 concentrations required to kill 50% of the cells in the experiment. For the skin abscess
1127 and peritonitis/sepsis infection mouse models, 10 mice per group, including 2 used for
1128 histological analysis, and 9 mice per group, respectively, were employed, in accordance
1129 with protocols approved by the University Laboratory of Animal Resources (ULAR) at
1130 the University of Pennsylvania.

1131

1132 **Statistical tests**

1133 In the intracellular antimicrobial activity assays and mouse experiments, all raw data were
1134 transformed using a log10 scale. Statistical significance at each time point was assessed
1135 independently using one-way ANOVA, followed by Dunnett's test for intracellular
1136 antimicrobial activity and Tukey's test for mouse experiments. P-values are reported for
1137 each group, with all groups compared to the untreated control group.

1138

1139 **Statistical analysis**

1140 All calculation and statistical analyses of the experimental data were conducted using
1141 GraphPad Prism v.10.3. Statistical significance between different groups was calculated
1142 using the tests indicated in each legend.

1143

1144 **Supplementary Information**

1145 Figures S1 to S11
1146 Tables S1 to S4
1147 References
1148